Simulation of two-phase liquid-vapor flows using a high-order compact finite-difference lattice Boltzmann method

Kazem Hejranfar* and Eslam Ezzatneshan
Aerospace Engineering Department, Sharif University of Technology, Iran
(Received 25 January 2015; revised manuscript received 13 July 2015; published 23 November 2015)

A high-order compact finite-difference lattice Boltzmann method (CFDLBM) is extended and applied to accurately simulate two-phase liquid-vapor flows with high density ratios. Herein, the He-Shan-Doolen-type lattice Boltzmann multiphase model is used and the spatial derivatives in the resulting equations are discretized by using the fourth-order compact finite-difference scheme and the temporal term is discretized with the fourth-order Runge-Kutta scheme to provide an accurate and efficient two-phase flow solver. A high-order spectral-type low-pass compact nonlinear filter is used to regularize the numerical solution and remove spurious waves generated by flow nonlinearities in smooth regions and at the same time to remove the numerical oscillations in the interfacial region between the two phases. Three discontinuity-detecting sensors for properly switching between a second-order and a higher-order filter are applied and assessed. It is shown that the filtering technique used can be conveniently adopted to reduce the spurious numerical effects and improve the numerical stability of the CFDLBM implemented. A sensitivity study is also conducted to evaluate the effects of grid size and the filtering procedure implemented on the accuracy and performance of the solution. The accuracy and efficiency of the proposed solution procedure based on the compact finite-difference LBM are examined by solving different two-phase systems. Five test cases considered herein for validating the results of the two-phase flows are an equilibrium state of a planar interface in a liquid-vapor system, a droplet suspended in the gaseous phase, a liquid droplet located between two parallel wettable surfaces, the coalescence of two droplets, and a phase separation in a liquid-vapor system at different conditions. Numerical results are also presented for the coexistence curve and the verification of the Laplace law. Results obtained are in good agreement with the analytical solutions and also the numerical results reported in the literature. The study shows that the present solution methodology is robust, efficient, and accurate for solving two-phase liquid-vapor flow problems even at high density ratios.

DOI: 10.1103/PhysRevE.92.053305 PACS number(s): 47.11.−j

I. INTRODUCTION

Multiphase and multicomponent fluid flows are ubiquitous in nature, industry, and daily practices and therefore much attention has been given for years to study these flows. Existence of interfacial dynamics with high gradients is the main difficulty for studying of multiphase flows from both the physical and numerical viewpoints. Any phase interface boundary is mesoscopic by nature [1] and the segregation of two fluids is due to interparticle forces. In the past two decades, the lattice Boltzmann method (LBM), because of its mesoscopic and kinetic nature, has become a promising numerically robust technique for the simulation of multiphase flows and interfacial dynamics with the underlying microscopic physics. From a computational point of view, the lattice Boltzmann (LB) equation is hyperbolic, which can be solved locally and efficiently on parallel computers. Simplicity of programming and ease of considering microscopic interactions for modeling of additional physical phenomenon are the other advantages of the LBM. For these reasons, the LBM has been an attractive alternative computational technique to the traditional Navier-Stokes solvers, especially for modeling multiphase flows.

From the macroscopic point of view, the multiphase models for the LBM can be considered as diffuse interface methods [2,3]. In the diffuse interface methods, it is not required to track or capture the interface position. This feature is a great advantage for the multiphase LB methods compared to the traditional computational fluid dynamic models based on the discretization of macroscopic continuum (Navier-Stokes) equations. In the multiphase LB methods, the phase separation occurs automatically by the incorporation of interparticle interactions directly and the interface sharpening mechanisms are provided by the momentum forcing term. The diffuse interface of phase is spread on grid points and the surface tension is transformed into a volumetric force. This mesoscopic kinetic nature and no need to track the interface can provide many of advantages for the simulation of multiphase or multicomponent fluid flows by the multiphase LB methods compared to the macroscopic interface capturing methods [e.g., the volume-of-fluid (VOF) [4] and the level set [5] methods] or to the macroscopic front tracking methods (e.g., the boundary-fitted grid method [6]). The multiphase LB methods with diffuse interface characteristics are easier computational methods for simulating complicated topological interface changes in three-dimensional flows and there are particularly appropriate for phase change problems [7]. The computational cost of the multiphase LB methods is also lower than the interface capturing or interface tracking methods in Navier-Stokes based solvers [8]. Furthermore, the multiphase LB methods as diffuse interface methods are especially appropriate for modeling the problems that are tough for sharp interface methods, such as the coalescence of droplets.

Several popular models in the LBM have been proposed for simulating multiphase and multicomponent fluid flows. These models divide into four categories: the

*khejran@sharif.edu

color-gradient- [9,10], pseudopotential- [11–14], free-energy- [15–19], and kinetic-theory- [20–23] based models. The models in the first three categories have an origin in the kinetic theory so they can be derived by discretizing the continuous Boltzmann equation with certain approximations. These approximations sometimes may be unphysical and lead to the spurious current in the interfacial region or the lack of Galilean invariance. He *et al.* [20], proposed an improved multiphase LBM that is derived by systematically removing the unphysical approximations. The He-Shan-Doolen (HSD) model is linked to the kinetic theory of dense gases and the attractive forces between the molecules are considered in two terms for the description of the real fluids in the Boltzmann kinetic equation. The first term is the influence of a particle in the short-range around itself, which is described by considering the Enskog volume exclusion effect. The second one is the long-range attractions which are described by the effects of the nonideality of the fluid involved. Consequently, the implementation of the thermodynamical concept is more flexible in the HSD model compared to the previous LB based models introduced. In this model, the Maxwell equal-area reconstruction procedure is admitted correctly with the consistent temperature concept. Using the HSD approach also allows flexibility in the variation of the surface tension for simulating a wide range of multiphase flows. However, the numerically instability associated with the stiffness of the collision operator is a serious limitation of the original HSD model for simulating complex multiphase flows with moderate to high density ratios. The stability problem is partially improved in the modified HSD formulations proposed by He and coworkers [21–23]. Applying the stable and efficient numerical schemes for the advection and collision operators may also eliminate the instability problem of this model [3,24,25]. Several efficient multiphase LB models have been developed based on the HSD approach because this model has a solid physical foundation [7,21,25–28]. This confirmation is the reason why this model is selected in this study.

Undesirable feature of the multiphase LB methods is the existence of interfacial spurious velocities because of imbalance between stresses in the interfacial region which causes a parasitic current in the interface of phases. Several attempts have been made to identify the origin of such spurious velocities and to reduce their level [13,17,27,29–32]. These spurious currents can also be reduced with large viscous dissipation [33]; however, they never entirely disappear in the most cases. Another drawback of the LBM-based multiphase models is their limitation due to the numerical instability for simulating fluid flows with high density ratios. The density ratio of liquid-gas systems is usually larger than 100, and even the density ratio of water to air is about 1000. Several attempts performed in the literature to overcome this difficulty in the different multiphase LB models. Yuan and Schafer [13] demonstrated that the Shan-Chen model can achieve smaller spurious currents and thus higher density ratios by using more realistic equations of state. Inamuro *et al.* [34] proposed an interesting approach based on the free-energy-based model to solve high density ratios by using the projection method. Zheng *et al.* [35] also used a modified multiphase LBM to improve the efficiency of the free-energy model for simulating two-phase flows with a density ratio of 1000. The efforts to improve the stability of the HSD model at high density ratios are performed by using the stable numerical discretization methods [24,25,36]. Cheng *et al.* [24] discretized the LBM with the HSD model using a stable finite-difference scheme with the artificial dissipation and showed that the LB formulation is able to simulate two-phase flows at a density ratio 1000. Lee and Lin [36] and later Lee and Fischer [26] used alternative numerical schemes for the discretization of the spatial derivatives of the equation of LBM based on the two-phase HSD model. The results obtained by them show that the stability of the HSD-based LBM is improved for large density ratios up to 1000 and very small spurious currents are observed.

These studies have shown that the numerical schemes used for the discretization of the microscopic velocity space and the advection term in the LBM and also for the approximation of the density derivatives of the two-phase model implemented can affect the stability of the solution algorithm, particularly for the problem with high density ratios. Recently, Mattila *et al.* [37] showed that a discretization scheme with an appropriate order is necessary to avoid inconsistent mixing of multiphase model dynamics with the numerical errors in the LBM. They have simply explained that the root of spurious currents at the interface is the numerical errors due to the significant density gradients. These errors arise from the discretization scheme used in the LBM and the application of high-order LB stencils can reduce the spurious currents more effectively. Consequently, the numerical stability of the scheme can be improved by reducing the effect of numerical errors in the calculation of the molecular interactions.

Using the finite-difference based schemes is one of extensive efforts to eliminate or reduce the numerical errors and thus improve the stability of the LBM for simulating practical multiphase fluid flows. Teng and coworkers [24,25] showed that the stability problem of the HSD model for simulating two-phase flows with high density ratios can be alleviated by applying a robust numerical scheme for the advection and collision operator. They could stabilize unstable LB formulation with the use of the total variation diminishing (TVD) scheme based on the finite-difference discretization for simulating two-phase flows with moderate to high density ratios in the range of 100–1000. Cristea and coworkers [28,30] used a finite-difference discretization with flux limiter to stabilize the HSD-based LBM for simulating two-phase flows with high density ratios with small parasitic currents. Using the finite-difference lattice Boltzmann method (FDLBM) can also remove the obvious drawback of the standard LBM. Note that the solution methodology based on the standard LBM is restricted to use uniform Cartesian grids with equal spacing at unit CFL (Courant-Friedrich-Lewy) number [38]. As described above, the inherent instability at high density ratios in multiphase flows is also another limitation of this solution methodology. These two limitations in the standard LBM greatly limit its applications to solve engineering practical problems. The FDLBM is widely used to overcome these shortcomings of the standard LBM [39–44], because it is easy to implement and it has better numerical stability characteristics.

The previous FDLBM developed in the literature for simulating multiphase flows are based on traditional

second-order finite-difference schemes and they still have the stability problems due to the existence of the numerical errors. The simulation results of the HSD-based FDLBM studies [25,28] deviate from the analytical solution based on the theory of Maxwell construction at low temperature values. An accurate and practical numerical method based on the finite-difference LBM is therefore interested that does not contain these deficiencies. In FDLBM, one can apply high-order accurate numerical methods for improving the accuracy and performance of the solution. Recently, we have proposed and applied a high-order compact finite-difference lattice Boltzmann method to solve incompressible flows in Cartesian and curvilinear coordinates [45,46]. Compared with a great variety of numerical methods, compact finite-difference methods are indicated to be considerably more accurate with benefit of having good resolution characteristics and smaller computational stencil size required. It is expected that the high-order compact finite-difference schemes that have sufficient stencil in the interfacial region of multiphase flows with applying an appropriate filtering procedure can reduce the numerical errors and also the parasitic currents to improve the stability and robustness of the LBM for the problems with high density ratios.

The main objective of the present paper is therefore to extend and apply an accurate and robust finite-difference LBM-based solver for simulating two-phase flows with high density ratios. Herein, the spatial derivatives in the LB equation with the HSD model and also in the intermolecular interaction force term are discretized by using the fourth-order compact finite-difference scheme and the temporal term is discretized by the fourth-order Runge-Kutta scheme to provide an accurate and efficient multiphase flow solver. A high-order spectral-type low-pass compact nonlinear filter is used to ensure the numerical stability. A sensitivity study is performed to examine the effects of the numerical parameters on the accuracy and performance of the solution. The accuracy and performance of the high-order CFDLBM applied are examined by computing different two-dimensional (2D) two-phase flows. The results obtained are compared with the analytical solutions and also the available numerical results. It is shown that the solution procedure adopted here for simulating two-phase flows reduces the interfacial spurious velocities and therefore improves the accuracy and numerical stability of the solution of large-density-ratio problems.

The rest of the present paper is organized as follows: In Section II, the lattice Boltzmann method is presented in relation to the multiphase flows. In Section III, the high-order compact finite-difference discretization and the Runge-Kutta time-stepping scheme for the LB equation with the HSD model is given. The filtering scheme used is presented in Section IV. Section V is devoted to present the numerical results for the different two-phase flows to examine the accuracy and robustness of the solution of the compact finite-difference LBM applied. Finally, the some conclusions are drawn.

II. GOVERNING EQUATIONS

It has been shown that the high-order CFDLBM developed [45] provides more accurate solutions compared to the current LB methods. The main goal of this paper is

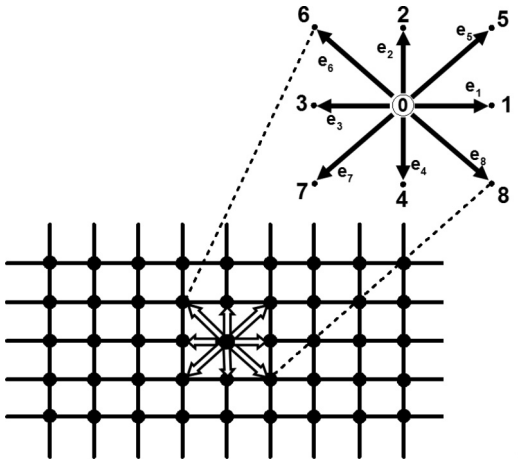

FIG. 1. The D2Q9 lattice and the microscopic velocities.

to extend the fourth-order CFDLBM for an accurate and efficient solution of the two-phase liquid-vapor flows. The dimensionless LB equation governed the particle distribution function $f(t,c,x)$ for isothermal nonideal gases is used [20] with the collision term in the Bhatnagar-Gross-Krook (BGK) approximation [47]

$$\frac{\partial f}{\partial t} + \boldsymbol{e}\cdot\nabla f + \mathbf{F}\nabla_{\boldsymbol{e}} f = -\frac{1}{\tau}(f - f^{\mathrm{eq}}), \tag{1}$$

where τ is the dimensionless collision relaxation time, $\boldsymbol{e}$ is the microscopic velocity of the particle, $\mathbf{F}$ is an external body force to which the molecules are exposed, and f^{eq} is the equilibrium distribution function. Since the derivative $\frac{\partial f}{\partial \boldsymbol{e}}$ cannot be calculated directly, the equilibrium distribution function f^{eq} is taken as the leading part of the distribution function f to approximate this derivative as [20,48]:

$$\nabla_{\boldsymbol{e}} f \approx \nabla_{\boldsymbol{e}} f^{eq} = -\frac{\boldsymbol{e}-\boldsymbol{u}}{c_s^2} f^{eq}. \tag{2}$$

In this approximation, it is assumed that the system is not too far from the equilibrium state. Here, $c_s = c\sqrt{\chi}$ is the sound speed of the LB model, $c = \sqrt{T/\chi}$ is the propagation speed of particles moving between a lattice node and its nearest neighbors, and χ is a characteristic of the LB model with a constant value. For the D2Q9 model, the value of χ is set to be $\chi = 1/3$ [14]. Also, T is the dimensionless system temperature which is normalized by the temperature of fluid in the critical point T_c [27,49].

A two-dimensional square lattice model with nine velocity directions (D2Q9) is employed to discretize Eq. (1) in the lattice configuration. Figure 1 indicates a rectangular solution domain for the LB equation with the particle distribution function f_α in the direction of the microscopic velocity $\boldsymbol{e}_\alpha$. For the D2Q9 computational domain, the discrete LB equation for multiphase flows can be derived as [24]

$$\frac{\partial f_\alpha}{\partial t} + \boldsymbol{e}_\alpha\cdot\nabla f_\alpha = -\frac{1}{\tau}\left(f_\alpha - f_\alpha^{eq}\right) + \frac{(\boldsymbol{e}_\alpha - \boldsymbol{u})\mathbf{F}}{c_s^2} f_\alpha^{eq}, \quad \alpha = 0,1,\ldots,8, \tag{3}$$

where the subscript α denotes the direction of the particle speed. In the D2Q9 discrete Boltzmann model, the microscopic

velocities are given as

$$\boldsymbol{e}_\alpha = (e_{\alpha x}, e_{\alpha y}) = \begin{cases} (0,0) & \alpha = 0 \\ \left[\cos\left(\frac{\alpha-1}{2}\pi\right), \sin\left(\frac{\alpha-1}{2}\pi\right)\right]c & \alpha = 1,2,3,4. \\ \left[\cos\left(\frac{\alpha-5}{2}\pi+\frac{1}{4}\pi\right), \sin\left(\frac{\alpha-5}{2}\pi+\frac{1}{4}\pi\right)\right]\sqrt{2}\,c & \alpha = 5,6,7,8 \end{cases} \tag{4}$$

The equilibrium distribution function f^{eq} is chosen to satisfy the Navier-Stokes equations through a Chapman-Enskog expansion procedure. Accordingly, the equation of the equilibrium distribution function is expressed as [50,51]

$$f_\alpha^{eq} = \rho w_\alpha \left[1 + \frac{\boldsymbol{e}_\alpha \cdot \boldsymbol{u}}{c_s^2} + \frac{1}{2}\frac{(\boldsymbol{e}_\alpha \cdot \boldsymbol{u})^2}{c_s^4} - \frac{1}{2}\frac{|\boldsymbol{u}|^2}{c_s^2}\right], \tag{5}$$

where $\boldsymbol{u} = (u,v)$ is the velocity vector and the weight coefficient w_α for the D2Q9 model is given by

$$w_\alpha = \begin{cases} \frac{4}{9} & \alpha = 0 \\ \frac{1}{9} & \alpha = 1,2,3,4. \\ \frac{1}{36} & \alpha = 5,6,7,8 \end{cases} \tag{6}$$

The macroscopic fluid density ρ and the macroscopic velocity u are obtained from the following equations:

$$\rho = \sum_\alpha f_\alpha, \quad \rho\,\boldsymbol{u} = \sum_\alpha \boldsymbol{e}_\alpha\, f_\alpha. \tag{7}$$

The interparticle interaction force accounts for the phase separation in the two-phase flows. As mentioned in the introduction, there are different schemes for modeling this force in the LB based methods. For the simulation of liquid-vapor systems subjected to the gravitational acceleration **a** in this study, the force term **F** in Eq. (3) is given by [14,19,20,21,30,52]

$$\mathbf{F} = -\frac{1}{\rho}\nabla[p^i - p^w] + 3\kappa\nabla(\nabla^2\rho) + \mathbf{a}, \tag{8}$$

where the p^i is the nondimensional ideal equation of state (EOS)

$$p^i = \rho T \tag{9}$$

and the thermodynamic pressure p^w can be determined from the nondimensional van der Waals EOS for the nonideal fluid

$$p^w = \frac{\rho T}{1 - b\rho} - a\rho^2. \tag{10}$$

This model was developed by He *et al.* [20] and it is known as the HSD model. They selected **F** by considering the intermolecular attraction and the effects of the exclusion volume of the molecules on the equilibrium properties of dense gases [3]. In the HSD model, the mean-field theory is used for approximation of the incorporating molecular interaction forces which are used to model the phase segregation and the surface tension. The surface tension is modeled by the second term of **F**, which is associated to the interfacial stress. This term should balance the thermodynamic pressure gradient in the interface profile to maintain in the equilibrium. In Eq. (8), the parameter κ controls the surface tension σ which allowing the flexibility for studying the capillary effects by variation of this parameter [3].

Note that in the HSD model, the phase separation is induced by mechanical instability in the supernodal curve of the phase diagram. As a result, the HSD approach is more flexible for the implementation of the thermodynamical model, with the consistent temperature concept, admitting the correct Maxwell's equal area reconstruction procedure. The theory of Maxwell construction for nonideal equations of state (e.g., the van der Waals EOS) is used to obtain the vapor and liquid densities at an equilibrium state from a given $p - v$ line, called the phase coexistence curve [53]. Figure 2 is a sketch indicating the $p - v$ curve of a pure fluid with isothermal lines from the van der Waals EOS given by Eq. (10). If the fluid is supercritical, $T > T_c$, the isothermal $p - v$ curve is monotonic in which it cannot be distinguished the liquid and vapor phases. For the subcritical situation, $T < T_c$, the $p - v$ curve for the EOS is no longer monotonic. This allows the coexistence of different densities for the fluid at a single pressure (three values for the density in the points A, B, and C) and there exists a mechanically unstable region when $(\frac{dp}{dv})_T > 0$. This condition indicates that for $T < T_c$, the liquid-vapor phase separation can occur; however, the van der Waals EOS fails to describe the fluid behavior in this region. To fix this problem, Maxwell [53] replaced the isothermal curve between A and C with a horizontal line positioned so the areas of the two hatched regions are equal (the Maxwell construction). This flat line corresponds to a liquid-vapor equilibrium condition and the value of liquid and vapor densities can be determined in the points A and C, respectively.

By considering the critical density ρ_c and the critical temperature T_c as the reference quantities of the liquid-vapor system, the constants a and b for the dimensionless van der Waals EOS, Eq. (10), can be given by [27]

$$a = \frac{9}{8}\frac{T_c}{\rho_c}, \quad b = \frac{1}{3\rho_c}. \tag{11}$$

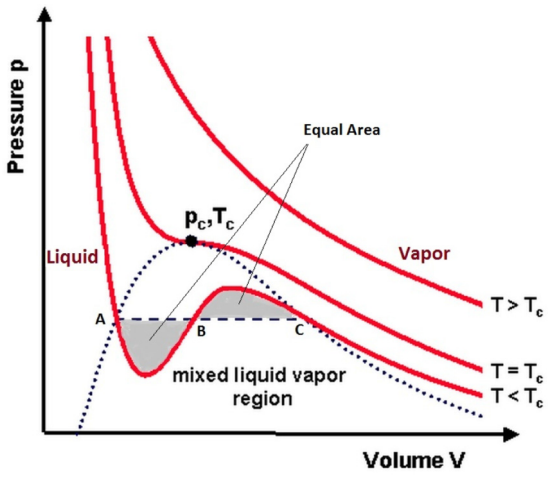

FIG. 2. (Color online) The Maxwell construction on the isothermal $p - v$ diagram.

The particle critical density is considered $\rho_c = 1$ at the critical temperature $T_c = 1$ [27]. Thus, the dimensionless van der Waals EOS can be rewritten as

$$p^w = \frac{3\rho T}{3-\rho} - \frac{9}{8}\rho^2. \tag{12}$$

With the van der Waals EOS in the form of Eq. (12), the critical point on the supernodal curve (Fig. 2) is located at the nondimensional temperature $T = 1$ and the non-dimensional density $\rho = 1$. Thus, $\rho > 1$ denotes the saturated liquid phase and $\rho < 1$ denotes the saturated vapor phase.

The numerical instability of the HSD model for the simulation of the complex fluids is a serious limitation of this approach. The instability is related to the stiffness of the collision operator, when the effects of complex fluids are introduced through the forcing term. This stability problem can be alleviated by providing robust numerical schemes particularly for the advection and collision operators [3,25]. A Chapman-Enskog expansion procedure up to second order shows that the Navier-Stokes equations can be derived from Eq. (3) [3,54],

$$\frac{\partial \rho}{\partial t} + \nabla \cdot (\rho \mathbf{u}) = 0, \tag{13}$$

$$\frac{\partial(\rho \mathbf{u})}{\partial t} + \nabla \cdot (\rho \mathbf{u}\mathbf{u}) = -\nabla p^w + \kappa\rho\nabla(\nabla^2\rho) + \rho\mathbf{a} + \nabla \cdot [\rho\nu(\nabla\mathbf{u} + \mathbf{u}\nabla)], \tag{14}$$

where the term $-\nabla p^w + \kappa\rho\nabla(\nabla^2\rho)$ at the right-hand side of the momentum equation is related to the free-energy functional of the van der Waals fluid [55], $\rho\nu(\nabla\mathbf{u} + \mathbf{u}\nabla)$ is the viscous stress tensor, and ν is the physical value of the kinematic viscosity of the fluid. The relaxation time τ for the finite-difference LB model is defined by [42]

$$\tau = \frac{\nu}{c_s^2}. \tag{15}$$

This expression of the kinematic viscosity and the relaxation parameter relation shows that the behavior of the fluid is independent of the discretization of the velocity space in the finite-difference based LB methods.

III. COMPACT FINITE-DIFFERENCE SCHEME FOR TWO-PHASE LBM

In this paper, the multiphase form of the LB equation, Eq. (3), is solved by a high-order compact finite-difference scheme. The main advantage of the finite-difference based schemes for the solution of the LB equation over the streaming-collision procedure in the standard LBM formulation is that they give more freedom to choose the discretization procedure in space and time, since the space steps $\Delta x, \Delta y$ and the time step Δt are no more related via the lattice speed. Another drawback of the standard streaming-collision formulation is that this procedure is limited to the second-order accuracy and it may not be suitable for studying complex flow physics that need to apply more accurate numerical schemes. Most of the finite-difference LB models developed in literature to solve two-phase fluid flows are also limited to second-order accuracy. In this study, the spatial derivatives in the two-phase LB equation are discretized by a fourth-order compact finite-difference scheme to obtain high-accuracy solutions. The LB equation (3) can be written in the following form by considering the spatial derivatives in the two-dimensional Cartesian coordinates:

$$\frac{\partial f_\alpha}{\partial t} = R(f_\alpha), \tag{16}$$

where

$$R(f_\alpha) = -\left(e_{\alpha x}\frac{\partial f_\alpha}{\partial x} + e_{\alpha y}\frac{\partial f_\alpha}{\partial y}\right) - \frac{1}{\tau}\left(f_\alpha - f_\alpha^{eq}\right) + \frac{(e_{\alpha x} - u)F_x + (e_{\alpha y} - v)F_y}{c_s^2} f_\alpha^{eq}. \tag{17}$$

An explicit multistage time-stepping method is used to discretize the temporal term in Eq. (16). Here the solution is advanced in the time t using a four-stage Runge-Kutta scheme. By integrating Eq. (16) with respect to the time t with the explicit fourth-order Runge-Kutta scheme, one can obtain

$$\begin{aligned} f_\alpha^0 &= f_\alpha^t \\ f_\alpha^k &= f_\alpha^0 + \zeta_k\,\Delta t\, R^{k-1}(f_\alpha), \quad k = 1,2,3,4, \\ f_\alpha^{t+\Delta t} &= f_\alpha^4 \end{aligned} \tag{18}$$

where Δt is the time step size and the parameters ζ_k ($k = 1,2,3$ and 4) are taken as $\frac{1}{4}$, $\frac{1}{3}$, $\frac{1}{2}$, and 1, respectively. The fourth-order Runge-Kutta time integration scheme is appropriate for an accurate calculation of unsteady flows [45,56].

Now the first derivative of the distribution function f_α in the x direction (denoted by $f'_\alpha = \partial f_\alpha/\partial x$) is computed with the fourth-order compact finite-difference scheme as [57,58]

$$f'_{\alpha,i-1} + 4f'_{\alpha,i} + f'_{\alpha,i+1} = \frac{3}{\Delta x}(f_{\alpha,i+1} - f_{\alpha,i-1}) + O(\Delta x^4), \tag{19}$$

where Δx is the lattice length unit. Equation (19) is applied in the computational domain for the grid points $i = 2,\ldots,I_{\max-1}$ for each j. To form the tridiagonal system of equations during the i sweep, appropriate boundary conditions are to be applied for the terms $f'_{\alpha,1}$ and $f'_{\alpha,I_{\max}}$.

For the periodic boundary conditions considered in the liquid-vapor systems studied in this paper, the terms $f'_{\alpha,1}$ and $f'_{\alpha,I_{\max}}$ at the boundary points can be calculated with the same procedure for the grid points in the computational domain mentioned in Eq. (19),

$$f'_{\alpha,I_{\max-1}} + 4f'_{\alpha,1} + f'_{\alpha,2} = \frac{3}{\Delta x}\left(f_{\alpha,2} - f_{\alpha,I_{\max-1}}\right) + O(\Delta x^4), \tag{20}$$

$$f'_{\alpha,I_{\max-2}} + 4f'_{\alpha,I_{\max-1}} + f'_{\alpha,1} = \frac{3}{\Delta x}\left(f_{\alpha,1} - f_{\alpha,I_{\max-2}}\right) + O(\Delta x^4). \tag{21}$$

For the wall boundary points, these terms can be calculated with appropriate one-sided compact relations. In the present calculations, the following third-order one-sided boundary

condition formulas are used [59]

$$f'_{\alpha,1} + 2f'_{\alpha,2} = \frac{1}{2\Delta x}(-5f_{\alpha,1} + 4f_{\alpha,2} + f_{\alpha,3}) + O(\Delta x^3), \tag{22}$$

$$f'_{\alpha,I_{\max}} + 2f'_{\alpha,I_{\max-1}} = \frac{1}{2\Delta x}\left(5f_{\alpha,I_{\max}} - 4f_{\alpha,I_{\max-1}} - f_{\alpha,I_{\max-2}}\right) + O(\Delta x^3). \tag{23}$$

The above fourth-order compact formulas together with the Eq. (19) are used to compute $\partial f_\alpha/\partial x$ implicitly for $i = 1,\ldots,I_{\max}$ for each j. The first derivative of the distribution function f_α in the y direction (denoted by $f'_\alpha = \partial f_\alpha/\partial y$) in Eq. (17) is computed for $j = 1,\ldots,J_{\max}$ for each i in the same manner.

Note that the calculation of the macroscopic parameters in the force term $\mathbf{F}$ implies first- and third-order spatial derivatives to be computed by the fourth-order compact finite-difference method employed. The gradient of the pressure term in the force term $\mathbf{F}$, $\nabla[p^i - p^w] = \frac{\partial}{\partial x_j}(p^i - p^w)$, involves the first-order spatial derivatives and they are calculated with the same procedure described above. For calculating the gradient of the Laplacian of the density in the force term $\mathbf{F}$, $\nabla(\nabla^2\rho) = \frac{\partial}{\partial x_j}(\frac{\partial^2\rho}{\partial x_i \partial x_i})$, that involves the third-order spatial derivatives the tridiagonal compact finite-difference scheme is applied 3 times.

IV. FILTERING SCHEME

The centered high-order compact finite-difference schemes are nondissipative and are therefore sensitive to numerical instabilities due to the growth of high-frequency modes. These difficulties originate usually from grid nonuniformity, boundary conditions, and nonlinear flow features [60]. Spurious oscillations may be occurred when simulating multiphase flows and thus lead to instabilities. These instabilities may be observed when applying the high-order compact finite-difference scheme for solving the two-phase LB equation. The mentioned difficulties can be overcome by applying a spatial filtering to the solution of the distribution function f_α or to add an appropriate dissipation term to the LB equation (16). Recently, some works have been performed to link the LB method with filtering. Ricot *et al.* [61] proposed a stabilization procedure for LBM via the linear explicit filtering and they studied the behavior of several spatial filters in different LBM algorithms. Brownlee *et al.* [62] explained some classes of techniques to improve regularization of LBMs by modifying dissipation. We used a high-order implicit filtering technique based on the works of Visbal and Gaitonde [63] to damp high-frequency oscillations associated with the central differencing of the spatial derivatives in the LB equation [45,46].

All the above noncompact (explicit) and high-order compact (implicit) filters mentioned are designed to eliminate the high-frequency waves and they are linear, because they are independent of the function to be filtered. It is generally recognized that the linear filters have desirable properties for smooth flows; however, they encounter serious problems for flows containing the regions of strong gradients or discontinuities such as shock. In fact, the low-dissipation schemes indeed results in spurious Gibbs oscillations near the discontinuities due to spectral truncation in the wave-number space. Thus, it is expected to observe some oscillations by implementing of the high-order compact finite-difference scheme with linear filters for the numerical solution of the two-phase flows, due to existing noticeable density gradients in the interface region. In order to prevent the appearance of Gibbs oscillations in the simulation of such flows, the nonlinear filters are to be applied [64–68]. The nonlinear filters are designed to detect the region of discontinuity by the implementation of a switch to active a suitable filtering procedure in the discontinuity regions of the computational domain and in the everywhere else.

There are good reasons that the second-order linear filter is suitable for discontinuity regions which are not the case for the higher-order linear filters. Some nonlinear filtering schemes designed based on this idea which have effective treatment near the discontinuity by switching to a second-order filter, but behave as a high-order linear filter in smooth regions [66–68]. Thus, the second-order filter has had negligible influence in the smooth region where the high-order linear filters have desirable properties. In this regard, a weighted essentially nonoscillatory (WENO)-type smoothness criterion is used by Visbal and Gaitonde [66] to define buffer zones for activating the second-order filter. Bogey *et al.* [67] utilized a sensor based on the high-frequency content of the pressure to switch between a second-order and a higher-order filter in discontinuity regions of the domain and in the everywhere else, respectively. Recently, Mahmoodi Darian *et al.* [68] proposed a sensor based on an order analysis and a suitable smoothness measurement to properly switch between a second-order and a higher-order filter.

In the present study, the high-order finite difference LB method by the implementation of nonlinear filters based on the works of Refs. [66–68] are used to solve the two-phase liquid-vapor systems with high-density ratios. In this regard, the filtered distribution function $\hat{f}_\alpha$ is calculated as a combination of the second- and a higher-order filtered distribution function:

$$\hat{f}_\alpha = \omega_1 \hat{f}^{(1)}_\alpha + \omega_m \hat{f}^{(m)}_\alpha, \quad m > 1, \tag{24}$$

where ω_1 and ω_m are the nonlinear weights controlling the amount of the second- and $2m$th-order filters. These weights are designed to preserve high accuracy of the filtered variable in smooth regions and to obtain a nonoscillatory sharp interface

$$\begin{aligned} &\omega_1 \approx 1, \quad \omega_m \approx 0 \text{ near interface regions,} \\ &\omega_1 \approx 0, \quad \omega_m \approx 1 \text{ in smooth regions.} \end{aligned} \tag{25}$$

According to these considerations, three different sensors are used here to determine the weights of the nonlinear filter on the interface and smooth regions. For a liquid-vapor system, there are several choices for the sensor variable, i.e., the density. However, for two reasons it is preferred to select the distribution function f_α as the sensor variable. First, the distribution function is the main variable involved in the numerical solution, and, second, the filter is directly applied to f_α.

Based on the WENO-type sensor of Visbal and Gaitonde [66], a central stencil of the fifth-order WENO scheme along with the distribution function is used to detect

the interface region

$$\Phi_j = \left[\tfrac{13}{12}(f_{\alpha,j+1} - 2f_{\alpha,j} + f_{\alpha,j-1})^2 + \tfrac{1}{4}(f_{\alpha,j+1} - f_{\alpha,j-1})^2\right]^2. \tag{26}$$

Using this sensor, named the SW sensor for the simplicity, the interface region is defined by

$$\Psi_j = \begin{cases} 1, & \Phi_j > \Phi_{th} \\ 0, & \text{else} \end{cases}, \tag{27}$$

where Φ_{th} is a specified threshold parameter which has been suggested to be set between 10^{-4} and 10^{-6}. In this study, the threshold parameter $\Phi_{th} = 10^{-6}$ is used for all the simulations. The points where $\Psi_j = 1$ correspond to the interface region. Thus, the weights of the second- and high-order filters in Eq. (24) are defined as

$$\omega_1 = \max(\Psi_j, \Psi_{j+1}), \quad \omega_m = 1 - \omega_1. \tag{28}$$

Another sensor is used based on the work of Bogey *et al.* [67], called the SB sensor, to determine the interface region. This sensor is applied in three steps. At first, we calculate

$$Df_{\alpha,j} = \tfrac{1}{4}(-f_{\alpha,j+1} + 2f_{\alpha,j} - f_{\alpha,j-1}). \tag{29}$$

The magnitude of the high-pass filtered distribution function is then calculated as

$$Df^{\text{magn}}_{\alpha,j} = \tfrac{1}{2}[(Df_{\alpha,j} - Df_{\alpha,j-1})^2 + (Df_{\alpha,j} - Df_{\alpha,j+1})^2] \tag{30}$$

and the interface sensor is defined as the ratio r expressed as

$$r_j = \frac{Df^{\text{magn}}_{\alpha,j}}{f^2_{\alpha,j}} + \varepsilon, \tag{31}$$

where $\varepsilon = 10^{-16}$ is introduced to avoid division by zero in the following expression:

$$\sigma_j = \frac{1}{2}\left(1 - \frac{r_{th}}{r_j} + \left|1 - \frac{r_{th}}{r_j}\right|\right). \tag{32}$$

For $r_j \leqslant r_{th}$, the filtering magnitude is $\sigma_j = 0$ and for $r_j > r_{th}$, it gets $0 < \sigma_j < 1$. In this way, the second-order filter is only switched on when the gradients of the distribution function is strong enough. The threshold parameter r_{th} has been suggested to be set between 10^{-4} and 10^{-6}. The lower value of this parameter leads to smoother solution in the interface region. In this study, the threshold parameter $r_{th} = 10^{-6}$ is used for all the simulations. The value of σ_j is used to define the weights of the second- and high-order filters in Eq. (24) as

$$\omega_1 = \max(\sigma_j, \sigma_{j+1}), \quad \omega_m = 1 - \omega_1. \tag{33}$$

The last sensor considered in this paper is the interpolation-based sensor (the IB sensor) according to the work of Mahmoodi Darian *et al.* [68]. They have proposed the following weights for switching between the second- and high-order filters in Eq. (24):

$$\omega_1 = 1 - \omega_m, \quad \omega_m = \exp\left(-c_e e^2_{j+1/2}\right), \tag{34}$$

where c_e is a positive constant number between 0 and ∞. For $c_e = 0$, the nonlinear filter is reduced to the high-order linear filter and $c_e \to \infty$ corresponds to the second-order linear filter. Note that using a larger value of c_e removes the oscillations appeared near the high gradient regions; however, it may cause unwanted damping in the numerical solution. They have used this constant in the range of $c_e = 200$ to $c_e = 4000$ for a less dissipative solution and to remove strong oscillations, respectively. The smoothness measurement term $e_{j+1/2}$ is defined as

$$e_{j+1/2} = \max(e_j, e_{j+1}), \tag{35}$$

where

$$e_j = \frac{|\hat{F}_{\alpha,j} - F_{\alpha,j}|}{D_j} \tag{36}$$

and $\hat{F}_{\alpha,j} - F_{\alpha,j}$ is the difference between the interpolated and computed values of the sensor variable defined as

$$\hat{F}_{\alpha,j} - F_{\alpha,j} = -(-1)^{m'} \frac{(m')!(m')!}{(2m')!} (\Delta\nabla)^{m'} F_{\alpha,j} \tag{37}$$

and $2m'$ is the order of interpolation error. In this study, a second-order interpolation ($m' = 1$) is used to compute the term $\hat{F}_{\alpha,j} - F_{\alpha,j}$ in Eq. (36), based on the distribution function as the sensor variable

$$\hat{F}_{\alpha,j} - F_{\alpha,j} = \tfrac{1}{2}(f_{\alpha,j+1} - 2f_{\alpha,j} + f_{\alpha,j-1}). \tag{38}$$

The denominator D_j is a scaling value which is described as

$$\begin{aligned} D_j &= c_s S_g + (1 - c_s) S_l \\ S_g &= U^g_{\max} - U^g_{\min}, \quad S_l = U^l_{\max} - U^l_{\min}, \end{aligned} \tag{39}$$

where S_g and S_l are the global and local scales, respectively, where their maximum and minimum terms are defined as

$$\begin{aligned} U^g_{\max} &= \max_k(U_k), \quad U^g_{\min} = \min_k(U_k) \quad 1 \leqslant k \leqslant j_{\max} \\ U^l_{\max} &= \max_k(U_k), \quad U^l_{\min} = \min_k(U_k) \quad j - m' \leqslant k \leqslant j + m'. \end{aligned} \tag{40}$$

The parameter c_s is the scaling constant with a positive value smaller than unity. This constant has been suggested to be set between 0.1 and 0.01. Using very small values for c_s is reasonable only for fine grids [68]. In the present study, the constants c_e and c_s are taken to be 200 and 0.1, respectively. If different values are used, the values are given explicitly.

Furthermore, in order to define the second- and high-order filters in Eq. (24), the implicit filters obtain the filtered variables $\hat{f}_\alpha$ from the unfiltered values f_α by solving the following tridiagonal system of equations:

$$a_f \hat{f}_{\alpha,i-1} + \hat{f}_{\alpha,i} + a_f \hat{f}_{\alpha,i+1} = \sum_{n=0}^{N} \frac{a_{n,i}}{2}(f_{\alpha,i+n} + f_{\alpha,i-n}), \tag{41}$$

where $2N$ is the order of filter with a $2N + 1$ point stencil. The $N + 1$ coefficients, $a_n, n = 0, 1, \ldots, N$, are derived in terms of a_f with Taylor and Fourier-series analyses [58,60,63,69]. The high-order filter is typically selected to be at least two orders of accuracy higher than the difference scheme of the LB equation. In the present study, the sixth-order filter is utilized for the

TABLE I. Second- and sixth-order filter coefficients at interior points.

Order	a_0	a_1	a_2	a_3
$f[O(\Delta x^2)]$	$\frac{1+2\alpha_f}{2}$	$\frac{1+2\alpha_f}{2}$	0	0
$f[O(\Delta x^6)]$	$\frac{11+10\alpha_f}{16}$	$\frac{15+34\alpha_f}{32}$	$\frac{-3+6\alpha_f}{16}$	$\frac{1-2\alpha_f}{32}$

calculations in the smooth regions. Table I presents the filtering coefficients for the tridiogonal second- and sixth-order filters. The parameter a_f satisfies the inequality $-0.5 < a_f < 0.5$, in which a higher value of a_f indicates a less dissipative filter. For the problems with the periodic boundary conditions, the filtering procedure mentioned in Eq. (41) can be used at the boundary points. For the problems with the wall boundary conditions special relations are needed at near wall boundary points due to the relatively large stencil of the filter. Note that the distribution function f_α at the wall boundary points, i.e., $i = 1, I_{\max}$, are not filtered. At near boundary points i, where Eq. (41) cannot be used, as proposed in Ref. [69], one can employ following higher order one-sided filter formulas

$$a_f \hat{f}_{\alpha,i-1} + \hat{f}_{\alpha,i} + a_f \hat{f}_{\alpha,i+1} = \sum_{n=1}^{7} a_{n,i} f_{\alpha,n} \quad i \in (2,3), \tag{42}$$

$$a_f \hat{\hat{f}}_{\alpha,i-1} + \hat{\hat{f}}_{\alpha,i} + a_f \hat{\hat{f}}_{\alpha,i+1} = \sum_{n=1}^{7} a_{I_{\max-n,i}} f_{\alpha,\, I_{\max-n}} \quad i \in (I_{\max-2},\, I_{\max-1}). \tag{43}$$

This boundary filter retains the tridiagonal form of the filter scheme and a_f remains as the only free parameter. In Table II, the coefficients for the sixth-order one-sided left-boundary filter formulas used in the present computations at the points 2 and 3 are given. The right-boundary formulas can be obtained by considering $a_{I_{\max-n,i}} = a_{n+1,I_{\max-n+1}}$ for $i \in (I_{\max-2}, I_{\max-1})$.

In the present calculations, the filtering procedure is applied sequentially in the x- and y-coordinate directions and the solution is filtered once after each time step of the algorithm. In the numerical results section, the accuracy and performance of the solution of the high-order compact finite-difference LB scheme by implementing the nonlinear filter with the SW, SB, and IB sensors are investigated for capturing the interface region of the two-phase flow problems studied. The stability and robustness of the numerical solution procedure implemented for the simulation of liquid-vapor flows with different values of density ratio are also examined for the different sensors in the nonlinear filtering procedure used.

V. IMPLEMENTATION OF BOUNDARY CONDITIONS

All the two-phase problems simulated here have either periodic or wall boundary conditions. The implementation of boundary conditions for the two-phase flows is nearly similar to that given in Refs. [45,46] for the incompressible flows. Note that the distribution function f_α is not given directly at the boundaries and a particular treatment should be applied to determine its value. The implementation of the periodic boundary conditions for calculating the distribution function f_α is straightforward, as given by Eqs. (20) and (21). For the wall boundaries, the boundary conditions of macroscopic variables are implemented at first and the distribution function f_α is then calculated based on them. Herein, the Dirichlet- or Neumann-type boundary conditions are used to define or update the macroscopic variables after each time step on the wall boundaries; the no-slip conditions for the velocity components ($u = v = 0$) are imposed and the density can be updated by considering $\partial\rho/\partial y_n = 0$ (y_n is the distance in the wall-normal direction) using the one-sided fourth-order finite-difference approximation as follows:

$$\rho_1 = \tfrac{1}{125}(240\rho_2 - 180\rho_3 + 80\rho_4 - 15\rho_5). \tag{44}$$

Now, Eqs. (16) and (17) are numerically solved at each wall boundary using the same algorithm employed for the interior points to determine the distribution function f_α at new time step on the wall boundary points. Note that the equilibrium part of the distribution function f_α^{eq} required in the LB equation (17) is determined by Eq. (5) with the use of the specified or updated macroscopic variables at the desired wall boundary. The terms $\frac{\partial f_\alpha}{\partial x}$ and $\frac{\partial f_\alpha}{\partial y}$ in LB equation (17) are also known from the compact differencing simultaneously at the interior and wall boundary points. The procedure given above can be applied to determine the distribution function f_α at each wall boundary. More details on the boundary conditions implementation have been presented in Refs. [45,46].

VI. NUMERICAL RESULTS

The accuracy and performance of the high-order accurate numerical scheme implemented to solve the multiphase LB equation are demonstrated for different two-phase liquid-vapor flow problems. Five test cases are considered for verifying the computations and assessing the solution methodology, namely the equilibrium state of a planar interface in a liquid-vapor system, a droplet suspended in the gaseous phase, a liquid droplet located between two parallel wettable surfaces, the coalescence of two droplets, and the phase separation in a liquid-vapor system at different conditions. Results obtained for these two-phase test cases by applying the CFDLBM are thoroughly compared and verified with those of the analytical solutions and the available numerical results. A sensitivity study is also performed to evaluate the effects of

TABLE II. Sixth-order filter coefficients at points 2 and 3.

Order	a_1	a_2	a_3	a_4	α_5	α_6	α_7
$f_2[O(\Delta x^6)]$	$\frac{1+62\alpha_f}{64}$	$\frac{29+6\alpha_f}{32}$	$\frac{15+34\alpha_f}{64}$	$\frac{-5+10\alpha_f}{16}$	$\frac{15-30\alpha_f}{64}$	$\frac{-3+6\alpha_f}{32}$	$\frac{1-2\alpha_f}{64}$
$f_3[O(\Delta x^6)]$	$\frac{-1+2\alpha_f}{64}$	$\frac{3+26\alpha_f}{32}$	$\frac{49+30\alpha_f}{64}$	$\frac{5+6\alpha_f}{16}$	$\frac{-15+30\alpha_f}{64}$	$\frac{3-6\alpha_f}{32}$	$\frac{-1+2\alpha_f}{64}$

grid size and filtering schemes implemented on the accuracy and performance of the solution of the two-phase compact finite-difference LBM applied.

A. The equilibrium state of a planar interface in a liquid-vapor system

When the temperature of a liquid-vapor system reaches below its critical value ($T < T_c$), phase separation occurs in the system. Thus, two different phases, a liquid phase with higher density and a gas phase with lower density, arise and the system get to equilibrium state in the new temperature. The 2D isothermal liquid-vapor system with a flat interface is a simple example of this type of two-phase flow with a phase separation. As a preliminary study, before addressing more complex problems, the simulation of the 2D plane interface is investigated to examine the efficiency of the fourth-order CFDLBM implemented by using three different sensors introduced for the filtering scheme. Cristea *et al.* [28] have used this test case to investigate the performance of the two different finite-difference schemes for the discretization of the LBM. They have implemented a first-order upwind (UP) scheme and also the second-order total variation diminishing (TVD) scheme with the monitorized central difference (MCD) flux limiter in their study. Their results obtained by the finite-difference LBM (FDLBM) show significant deviations from the theoretical densities of the two coexisting phases, particularly at low temperatures. The theoretical curve of the two coexisting phases is calculated according the Maxwell equal area construction [55]. The lowest temperatures in which the numerical schemes used by Cristea *et al.* remain stable for solving the phase separation are $T = 0.73$ and $T = 0.82$ for the UP and the MCD schemes, respectively. Teng *et al.* [25] have employed three second-order FDLBM schemes: the MacCormack scheme, the TVD scheme, and a new TVD with the artificial compression (TVD/AC) scheme to solve the 2D liquid-vapor system with flat interface. As in Cristea *et al.*, their results using the MacCormack and TVD schemes are not in agreement with the theoretical coexisting curve at the low temperatures. The MacCormack and TVD schemes used by them are numerically unstable for the temperatures below $T = 0.8$ and $T = 0.6$, respectively. However, the TVD/AC scheme remains stable for the lower temperatures until $T = 0.51$ in which the density ratio reaches 100 and the results obtained are in good agreement with the theoretical ones. The liquid-vapor system with the flat interface is also used by Wagner [70] to investigate the accuracy and performance of a LBM that implements a high-order scheme to discretize the fourth-order spatial derivatives in the nonideal terms of the LB equation. He imposed the nonideal terms through either forcing or pressure terms for the simulation of two-phase flows. He concluded that using a second-order discretization for the high-order spatial derivative terms in the nonideal LBM leads to a lack of thermodynamic consistency that prevents to obtain a true equilibrium solution for the liquid-vapor two-phase flows. Using the high-order discretization scheme for the nonideal fourth-order derivative terms in his proposed LBM leads to more accurate results for the liquid-vapor system with the flat interface compared with the theoretical coexisting curve. However, his proposed LBM with the high-order discretization

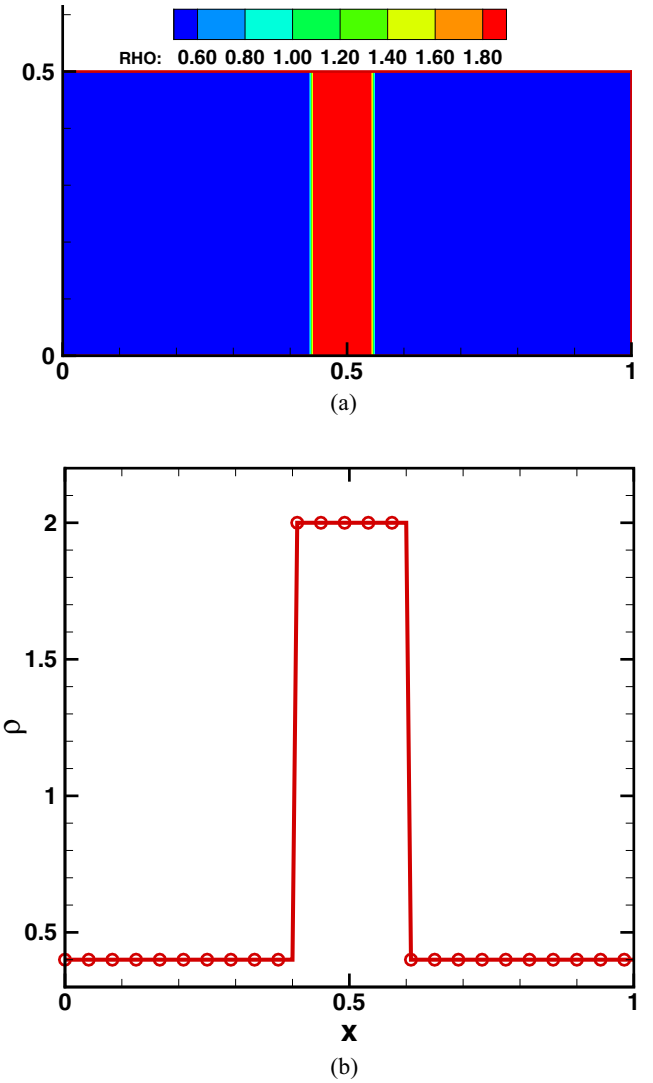

FIG. 3. (Color online) Initial condition (a) density contours and (b) sharp density profile at midplane for a 2D isothermal liquid-vapor system with a flat interface.

scheme is unstable for the temperatures below $T = 0.87$ (corresponds to the density ratio about 5) using both the forcing and pressure methods.

In the present study, the size of system is 1.0×0.5 with a 121×61 uniform computational grid. Periodic boundary conditions are applied to the all open boundaries at the four sides of the computational domain. The time step, relaxation factor, surface tension coefficient, and filtering coefficient are set to be $\delta t = 10^{-4}$, $\tau = 10^{-4}$, $\kappa = 10^{-4}$, and $a_f = 0.49$, respectively, except for special declarations. The initial density distribution contours and its sharp profile at the midplane of the 2D domain are shown in Fig. 3. In the middle of the domain, the density is initialized to be $\rho = 2$ and its value is set up $\rho = 0.4$ in the other parts. For the temperatures near the critical temperature value ($T \geqslant 0.6$), it takes about 15 dimensionless time for the liquid-vapor system established to reach the equilibrium state of the system using the two-phase compact finite-difference LBM applied. However, it needs to perform 25 dimensionless time to ensure the equilibrium

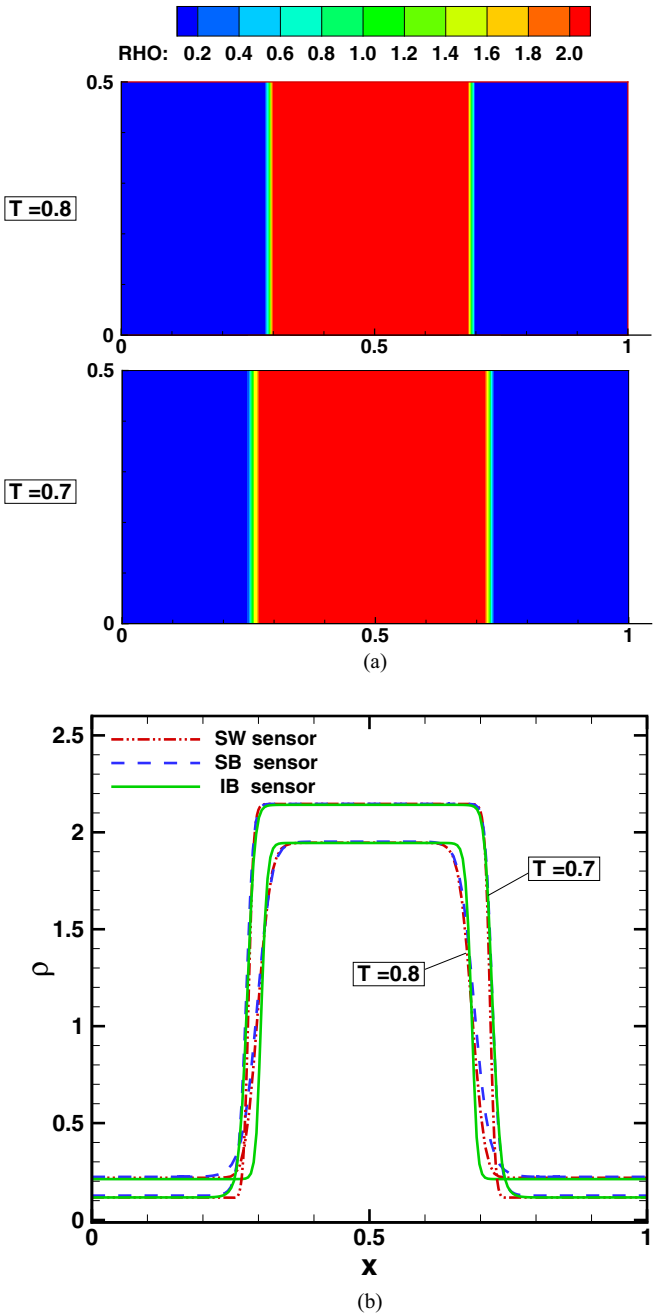

FIG. 4. (Color online) Computed (a) density field and (b) density profiles at midplane for a 2D isothermal liquid-vapor system with a flat interface using SW, SB, and IB sensors at temperatures $T = 0.8$ and $T = 0.7$.

state for lower temperatures ($T < 0.6$). Figure 4 shows the density contours and its profiles at the midplane of the 2D equilibrated liquid-vapor system with a flat interface for the SW, SB, and IB filtering sensors at the temperatures $T = 0.8$ and $T = 0.7$. As observed in this figure, the value of liquid and gas densities calculated are not significantly affected by the three different sensors used in the filtering scheme. Note that the IB sensor provides a slightly sharper interface in the density profile compared with the results of the SW and SB sensors at the temperature $T = 0.8$. The smoothness of the flat

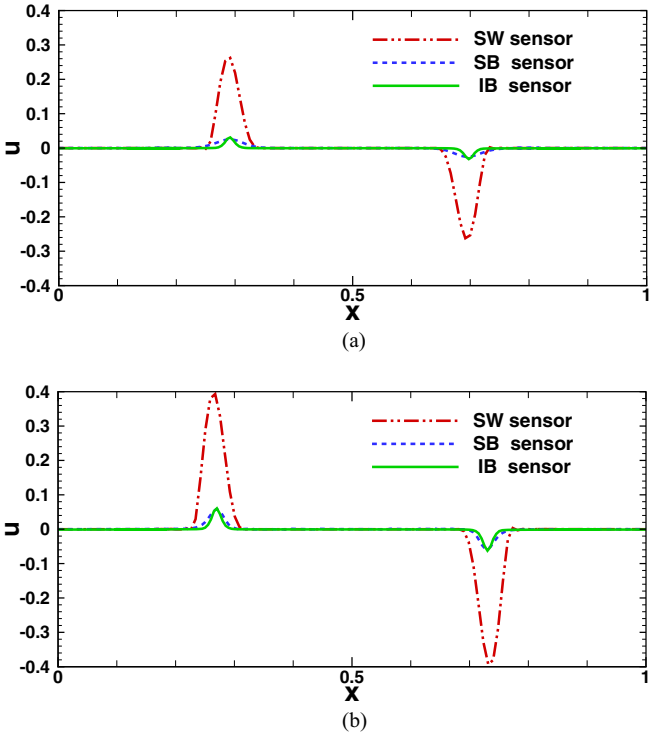

FIG. 5. (Color online) Comparison of velocity profiles at midplane for a 2D isothermal liquid-vapor system with a flat interface using SW, SB, and IB sensors at temperatures (a) $T = 0.8$ and (b) $T = 0.7$.

interfaces computed by the three sensors used are almost the same at the temperature $T = 0.7$.

The density profile of the liquid-vapor systems must be monotonic with respect to the position. Hence, zero velocities at the equilibrium state of the liquid-vapor systems are expected according to the mass conservation equation [Eq. (13)]. However, the existence of the spurious numerical terms in the momentum conservation equation causes an unbalance between the gradients of the pressure and the interfacial stress, which may produce nonzero velocities in the interface region [3,25]. The existence of the spurious velocities in the numerical simulations of the liquid-vapor systems using the standard LBM and FDLBM are previously reported by many researchers (e.g., see Refs. [25,27,71–73]). Figure 5 shows the velocity profiles in the midplane of the 2D equilibrated liquid-vapor system using the fourth-order compact finite-difference LBM implemented with the SW, SB, and IB sensors at the temperatures $T = 0.8$ and $T = 0.7$. By using the SW sensor, the maximum values of existing spurious velocities in the interface region are higher than those predicted by using the SB and IB sensors. The spurious velocities are found to be smaller when the IB sensor is applied in the filtering scheme compared to the SW and SB sensors. As seen in Figs. 4 and 5, with decreasing the temperature, the difference between the density of liquid and gas phases is increased and the magnitude of the spurious velocities becomes larger in the interface. Increasing the magnitude of the spurious velocities at the lower temperatures is the main reason of the instability of the numerical schemes based on the LBM to solve two-phase systems with high density ratios.

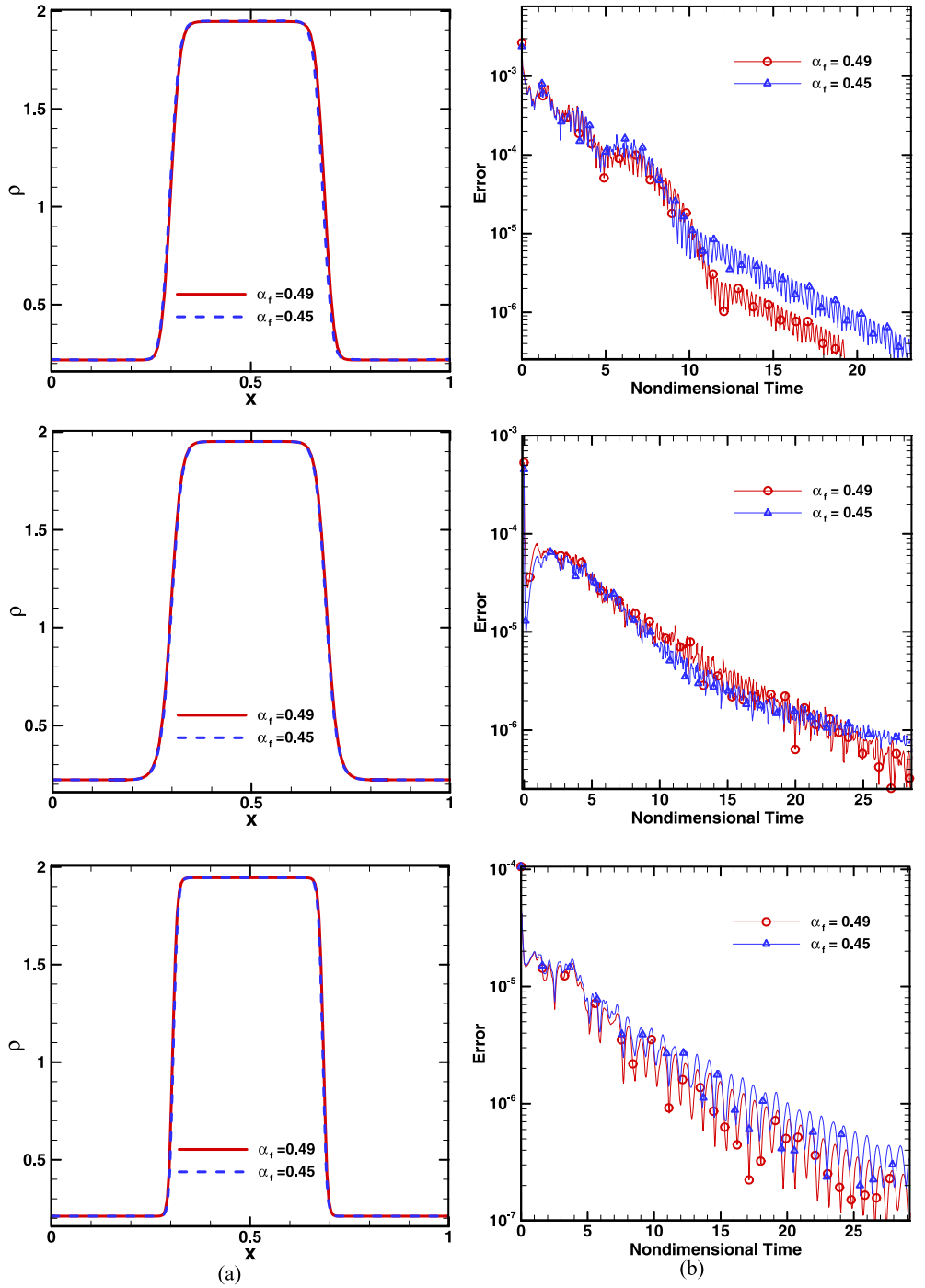

FIG. 6. (Color online) Effect of value of filter coefficient a_f on (a) density profile at mid-plane and (b) convergence rate of solution using SW sensor (top row), SB sensor (middle row), and IB sensor (bottom row) for a 2D isothermal liquid-vapor system with a flat interface at temperature $T = 0.8$.

A sensitivity study is conducted to investigate the effects of the value of the filtering coefficient α_f in the SW, SB, and IB sensors on the accuracy and convergence rate of the solution at $T = 0.8$. Figure 6 shows the density profiles at the midplane of the 2D domain for different values of filtering coefficient. It is indicated that the accuracy of the solution of the two-phase flow with the plane interface computed based on the compact finite-difference LBM is not affected by the value of the filtering coefficient. In this figure, the convergence history of the solution is also shown for the error of the u-velocity profile in the flow field at $T = 0.8$. The error is defined as the L_∞ norm of the u velocity in the flow field calculated by:

$$L_\infty = \max\left(\left|u_{i,j}^{n+1} - u_{i,j}^{n}\right|\right), \quad (i,j) = (1,1),\ldots,(I_{\max}, J_{\max}) \tag{45}$$

at the time steps n and $n+1$. The study indicates that the convergence rate of the solution is not also very sensitive to the value of the filtering parameter.

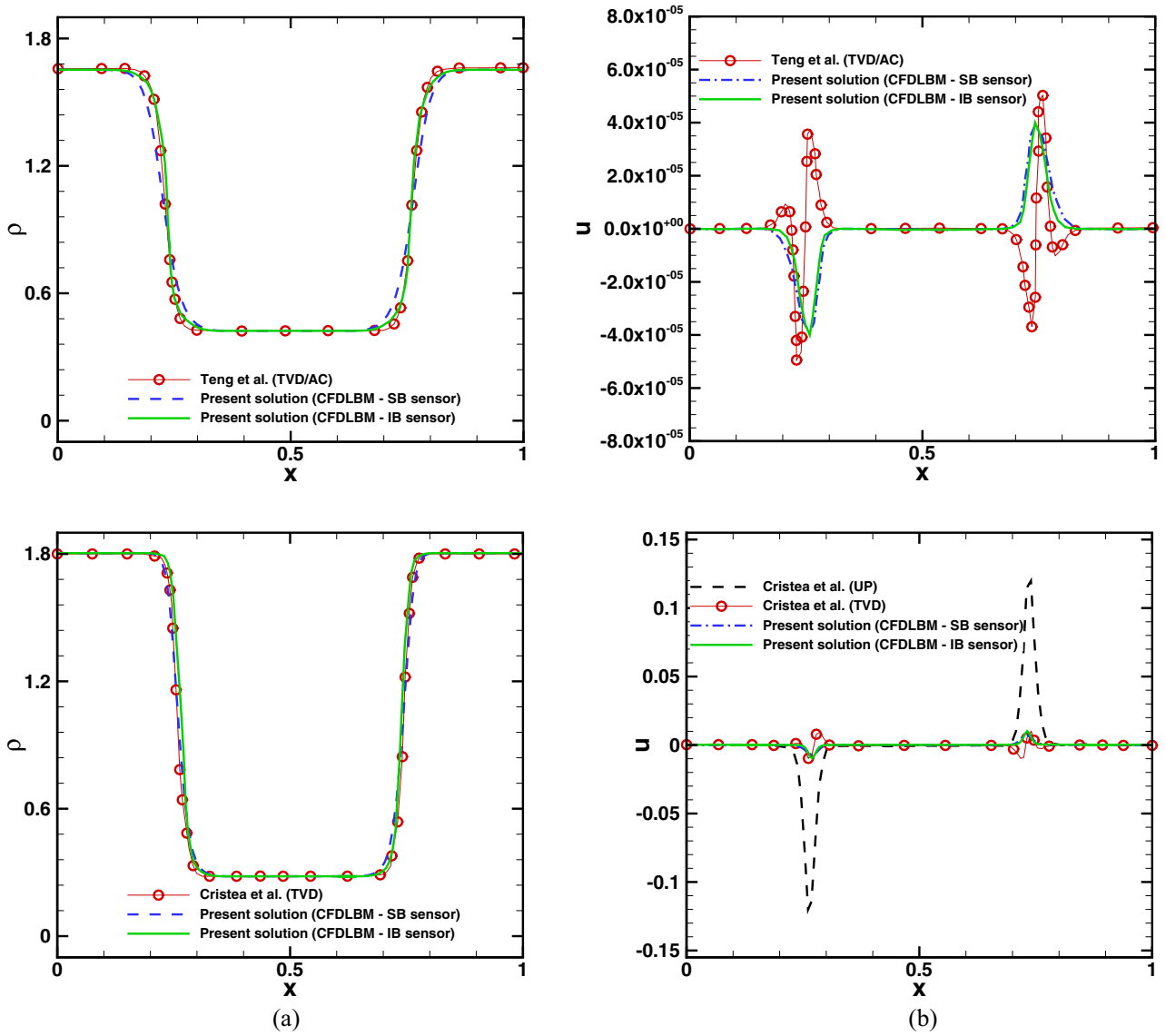

FIG. 7. (Color online) Comparison of (a) density and (b) velocity profiles at midplane for a 2D isothermal liquid-vapor system with a flat interface at $T = 0.9$, $\kappa = 2.5 \times 10^{-5}$ (top row) and $T = 0.85$, $\kappa = 10^{-5}$ (bottom row).

Figure 7 shows the comparison of the density and velocity profiles at the midplane of the 2D liquid-vapor system computed by the present solution procedure with the results reported by Teng *et al.* [25] and Cristea *et al.* [28] in two different conditions. The results obtained for the density profiles are in good agreement with the available numerical results. As shown in this figure, the present solution procedure reduces the numerical fluctuations of the solution in the interface region compared to those of the previous results reported in the literature. Such an improvement is because of implementation of the appropriate filtering schemes in the present solution procedure. It is found that the high-order compact finite-difference LBM applied has good stability characteristics for the simulation of the two-phase liquid-vapor flows with high density ratios.

The equilibrium state of the liquid-vapor system with a planar interface is solved in different temperatures below the critical temperature value to demonstrate the accuracy and performance of the present numerical scheme for the simulation of two-phase flows. Figure 8 shows the densities of the coexisting phases calculated in the equilibrium state at different values of temperature by using the compact finite-difference LBM implemented with the SW, SB, and IB sensors in the filtering scheme. The results obtained are verified with those of the theoretical values. As shown in this figure, the numerical results computed using all the three filtering procedures implemented agree very well with the theoretical curve at a wide range of density ratios. However, the two-phase compact finite-difference LBM implemented by using the SW sensor in the filtering scheme becomes numerically unstable for the temperatures below $T = 0.7$ which is equivalent to the liquid to vapor density ratio of $\rho_l/\rho_v = 18.4$. This instability problem is related obviously to the higher spurious velocities in the interfacial region obtained by using this sensor at lower temperatures, as shown in Fig. 5. By using the SB and IB sensors, however, the present numerical scheme becomes more

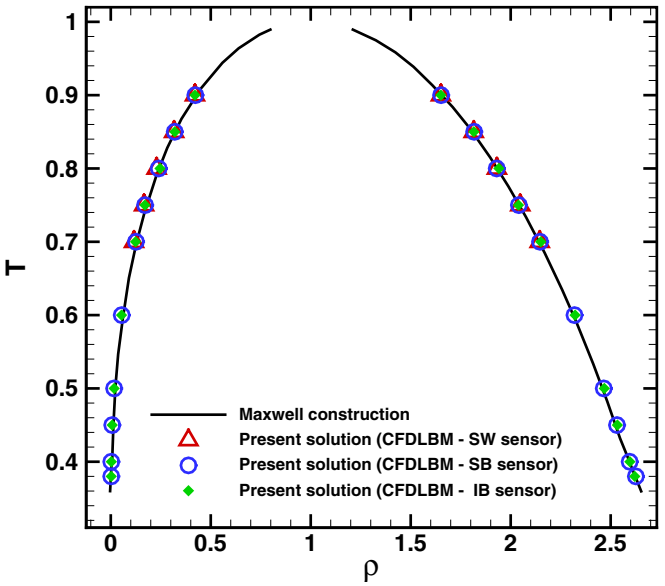

FIG. 8. (Color online) Coexistence curve for a 2D isothermal liquid-vapor system with a flat interface at different temperatures obtained by the present solution procedure using SW, SB, and IB sensors compared with the theory of Maxwell construction.

stable for the simulation of lower temperatures with larger density ratios. The two-phase compact finite-difference LBM implemented with the SB and IB sensors is still stable for the temperature $T = 0.38$, which is corresponds to the density ratio $\rho_l/\rho_v = 1141$ and 1091, respectively. According to the level of the spurious velocities predicted by using the SW, SB, and IB sensors (see Fig. 4), it is expected that the numerical scheme implemented be more stable by using the SB and IB sensors for the simulation of the liquid-vapor systems with the high density ratios. Table III compares the computed results for the liquid-to-vapor density ratio ρ_l/ρ_v by applying the SW, SB, and IB sensors in the filtering scheme at different temperatures. The highest density ratio is recovered with the SB sensor and it is significantly larger than the one obtained with the SW sensor. These results shows that the fourth-order compact finite-difference LBM by using the SB and IB sensors is robust

TABLE III. Comparison of density ratios of the planar interface liquid-vapor system calculated by implementation of SW, SB, and IB sensors at different temperatures.

	$\frac{\rho_l}{\rho_v}$		
T	SW sensor	SB sensor	IB sensor
0.90	3.92	3.90	3.92
0.85	5.73	5.68	5.67
0.80	8.42	8.06	7.89
0.75	12.29	11.90	11.93
0.70	18.44	17.05	17.34
0.60		42.39	43.15
0.50		147.62	145.19
0.45		346.79	342.38
0.40		961.11	927.17
0.38		1141.73	1091.88

and suitable for solving liquid-vapor flows even at high density ratios and provides accurate and efficient solutions. Due to the better performance of the compact finite-difference LBM with the SB and IB sensors, it is decided to adopt these two sensors for further simulations. It is noted that the van der Waals EOS used in this study for computing the pressure of nonideal fluids is the simplest and most famous equation of state. However, by replacing the van der Waals EOS with a more realistic equation, like the Redlich-Kwong EOS, a better performance can be achieved [13,74].

B. A droplet in gaseous phase

The 2D stationary droplet is an appropriate test case to verify various models for multiphase flows. Here this problem is solved to demonstrate the accuracy and performance of the present numerical scheme. In the present work, a doubly periodic domain $0 \leqslant x, y \leqslant 2$ is used and the time step, the relaxation factor, and the surface tension coefficient are set to be $\delta t = 10^{-4}$, $\tau = 10^{-4}$, and $\kappa = 10^{-4}$, respectively, except for special declarations. For this test case, the SB and IB sensors are used in the filtering scheme of the fourth-order CFDLBM implemented to ensure the stable solutions for the simulation of the stationary droplets with high density ratios. The filtering coefficient set to be $a_f = 0.49$. The initial condition of a droplet suspended in the gaseous phase is determined with the density distribution in the flow field at which the density profile is sharp in the interface. For the initialization of the simulations in this study, a circular region with the radius $R = 0.1$ at the center of the 2D domain is initialized with the density $\rho = 1.1$ and the density of the other parts of the domain is set to be $\rho = 0.2$. The calculations are performed for 30 nondimensional time to ensure the equilibrium state.

At first, a grid refinement study is performed at the temperature $T = 0.4$ to examine the sensitivity of the solution on the grid size. The computational grids used for these flow conditions are (101×101), (151×151), (201×201), and (301×301). Figure 9 shows both the density and u-velocity profiles along the midline through the center of the domain for the different meshes. As illustrated in this figure, the differences between the predicted density and velocity profiles for the grid (201×201) and the fine grid (301×301) are small and the solution seems independent of the grid size when the number of grid points becomes larger than the (201×201) one. The grid refinement study also indicates that the magnitude of the spurious velocities is decreased by increasing the number of grid points. This conclusion confirms that the discretization errors of the finite difference method employed to solve the LB equation are one of the reasons of existing the spurious velocities. Note that the discretization errors are as the one the reason of existing the spurious velocities in the liquid-vapor interfaces reported for both the standard LBM [31,32] and FDLBM [25,27]. Cristea and Sofonea [27] have introduced a correction force term to eliminate the discretization errors in the FDLBM with the first-order upwind scheme for reducing the spurious velocities in the liquid-vapor systems. In Table IV, the order of spatial accuracy of the solution for this test case is calculated by employing the SB sensor for $T = 0.4$ based on the maximum

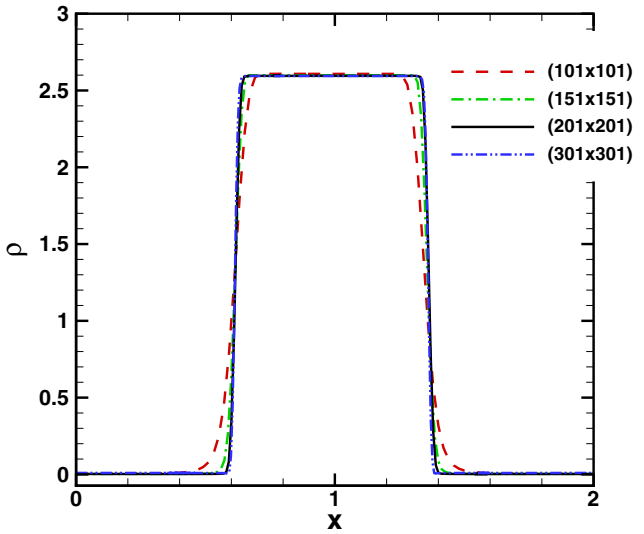

(a)

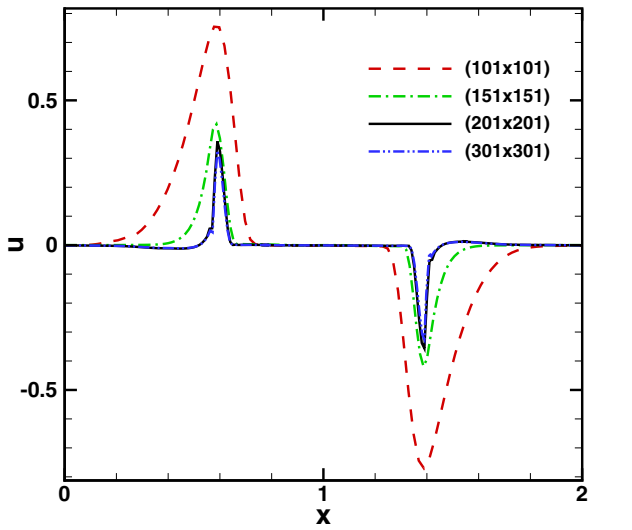

(b)

FIG. 9. (Color online) Grid refinement study on (a) density and (b) u-velocity profiles along midline through center of domain for 2D droplet suspended in gaseous phase at temperature $T = 0.4$.

value of the spurious velocity for all the grid points for the meshes (101 × 101), (151 × 151), and (201 × 201) compared with the results of the most refined one, the mesh (301 × 301). The order of spatial accuracy is about 3.77 that verifies the fourth-order accuracy of the numerical scheme implemented.

TABLE IV. Order of accuracy of the solution based on the maximum value of the spurious velocity in the interfacial region of a 2D droplet at $T = 0.4$.

Grid	Δx	Log(Δx)	Log(error)
(101 × 101)	2/100	–1.6989	–0.3693
(151 × 151)	2/150	–1.8750	–1.0423
(201 × 201)	2/200	–2.0000	–1.5040
Order of accuracy			∼ 3.77

Figure 10 illustrates the results for the equilibrium state of the circular droplet calculated using the present solution procedure by using the SB and IB sensors at different temperatures. The computed 2D liquid-vapor flow field are depicted by the density contours for $T = 0.4$, 0.6, and 0.8, recovered for $\kappa = 10^{-4}$ using the compact finite-difference LBM implemented. It is observed that the shape of droplets does not depart from a circle at the equilibrium state and their shape does not also change any longer after equilibrium condition. It is observed that the results obtained for both the SB and IB sensors are nearly the same. However, the interface region is slightly smeared by using the SB sensor for the temperature $T = 0.8$. To study this in detail, the variation of the density profile across the droplet interface at different temperatures is studied. In order to show and to clearly compare the interfaces, the interfacial region of the droplets at different temperatures are cut from the whole domain, as shown in Fig. 11. Figure 12 makes a comparison of the results obtained by using the SB and IB sensors. The density profiles in the interface region are nearly the same for different temperatures $T = 0.4$ to 0.7. However, as expected from Fig. 10, the SB sensor smooths the interface region more than the IB sensor, especially at the high-temperature value $T = 0.8$. The spurious velocity arising in the simulation of a circular droplet is investigated in the equilibrium state by the present solution procedure using the SB and IB sensors in different dimensionless temperatures. Figure 13 shows the comparison of the maximum value of the spurious velocity in the computational domain obtained based on the compact finite-difference LBM employed with the results reported by Yuan and Schaefer [13] based on the standard LBM using the two-phase Shan-Chen model. This figure shows that the present solution procedure reduces the magnitude of the spurious velocities compared to an ordinary two-phase LBM. Mattila *et al.* [37] also investigated the spurious currents for an equilibrated droplet at the dimensionless temperature $T = 0.9$ using the two-phase LBM with the high-order discretization schemes with implementing the HSD model. The magnitudes of the spurious velocity reported by Mattila *et al.* where 5.84×10^{-3}, 4.34×10^{-3}, and 6.63×10^{-4} using three discretization methods include a third-order backward differentiation formula (BDF), a third-order Adams–Moulton method (A-M), and a second-order trapezoidal LBE, respectively. The maximum values of the spurious velocity for an equilibrated droplet at the dimensionless temperature $T = 0.9$ obtained by the high-order compact finite-difference LBM presented using the SB and IB sensors are 3.72×10^{-5} and 3.31×10^{-5}, respectively, are at least one order of magnitude lower than those of reported by Mattila *et al.* The low spurious currents will make the simulations based on the present numerical scheme implemented be stable for the solution of the liquid-vapor two-phase flows even at high density ratios.

Now a sensitivity study is conducted to ensure that the constants in the IB sensor do not affect the accuracy of the solution at $T = 0.8$. Figure 14 shows the density profiles at the interface region for different values of the c_e and c_s in the IB filtering scheme compared with the result of the SB sensor. It is indicated that the accuracy of the solution computed based on the compact finite-difference LBM employed by using the IB sensor is not affected by the value of the filtering constants.

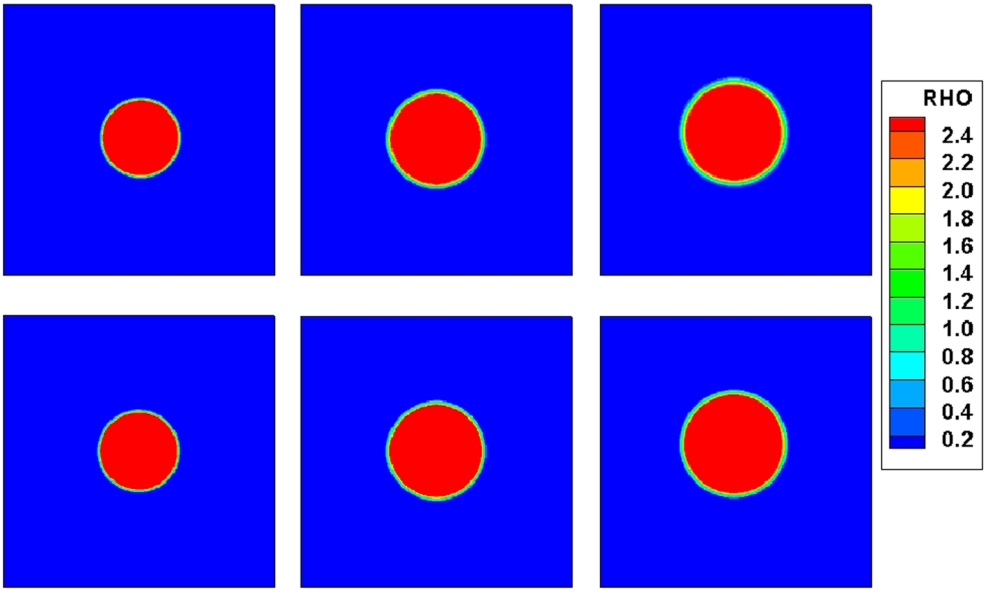

FIG. 10. (Color online) Comparison of computed density field of equilibrium state of 2-D droplet using SB sensor (top row) and IB sensor (bottom row) at temperatures (a) $T = 0.4$, (b) $T = 0.6$, and (c) $T = 0.8$.

Figure 12 also shows that the interface thickness decreases with decreasing the temperature and the density profile becomes sharper. The thicker interface of the droplet with increasing the temperature is also clearly observed in Fig. 10. In fact, with the decrease of the temperature, the surface tension is increased and, as expected, the liquid-to-vapor density ratio increases. As in the previous study for liquid-vapor systems with the plane interface, this study also indicates that the compact finite-difference LBM implemented using the SB and IB sensors is numerically stable for the solution of the two-phase flows with the curve interface for high density ratios about $\rho_l/\rho_v = 1000$ which is equivalent to the temperature about $T = 0.4$.

Similarly, the density profile is also studied for different values of surface tension coefficient κ by using the SB and IB sensors at the same temperature $T = 0.5$. Figure 15 illustrates that the value of the density calculated for the liquid and vapor phases does not change for different values of surface tension coefficient κ. However, the interface width becomes larger as κ increases and the transition region between the two phases is smooth. The results indicated in Figs. 12 and 15 verify that the density ratio between the liquid and the vapor phase is only determined by the temperature.

The satisfaction of the Laplace law [55] is an important benchmark test for the validation of the droplet suspended in

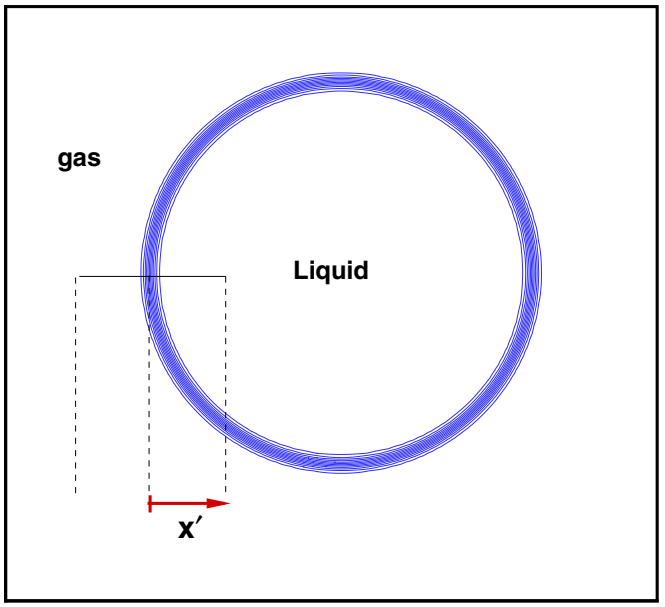

FIG. 11. (Color online) A schematic of cut-off zone in interfacial region of 2D droplet.

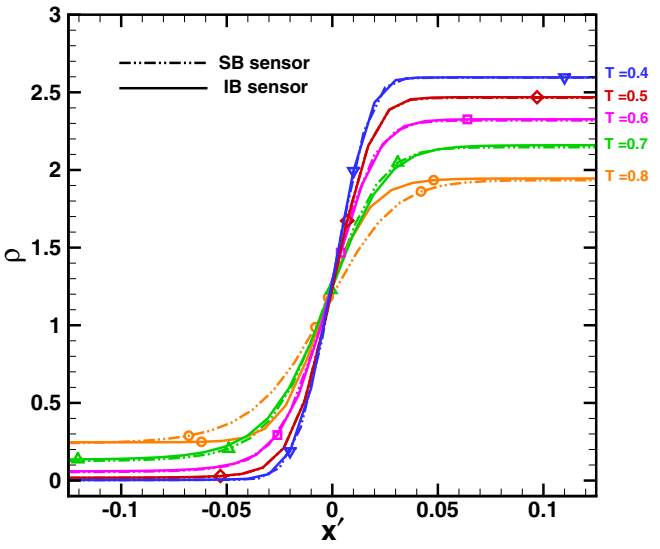

FIG. 12. (Color online) Comparison of density profiles at interfacial region of 2D droplet using SB and IB sensors at different temperatures.

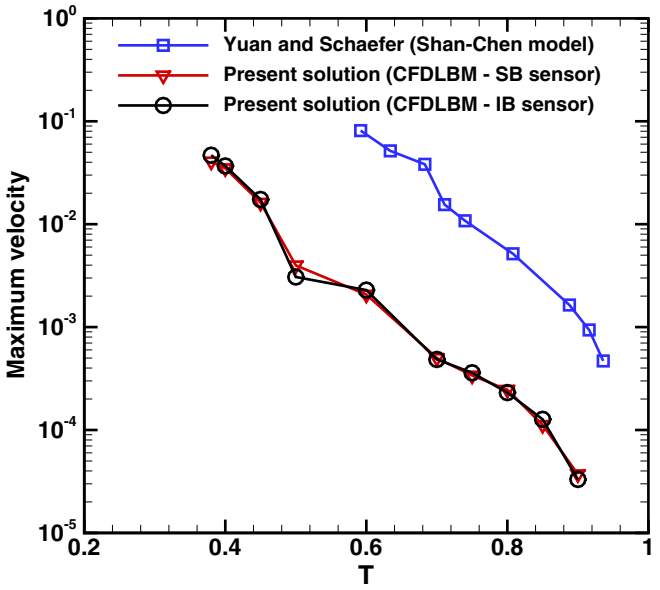

FIG. 13. (Color online) Comparison of maximum value of spurious velocity for equilibrium state of 2D droplet calculated by the present solution procedure using SB and IB sensors with the standard Shan-Chen model at different temperatures.

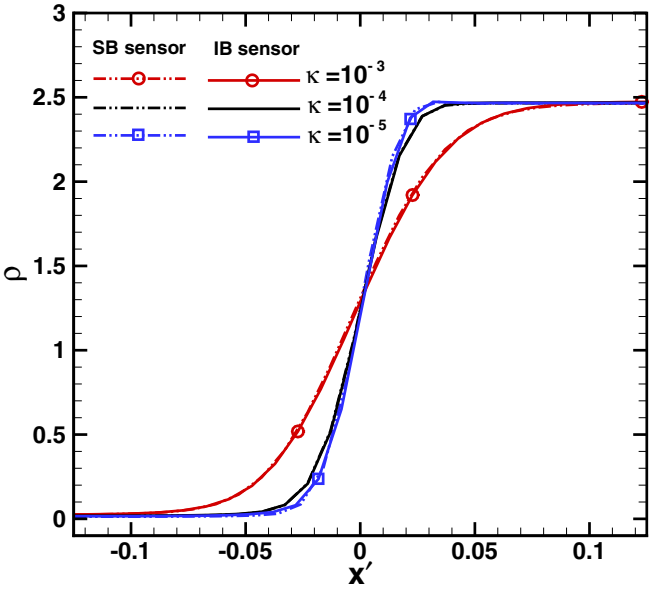

FIG. 15. (Color online) Effect of value of surface tension coefficient κ on density profiles at interfacial region of 2D droplet using SB and IB sensors at temperature $T = 0.5$.

the gas. According to the Laplace law, the tension in the surface makes a pressure difference Δp between the inside and outside of the droplet. Thus, the interfacial tension can be evaluated based on the Laplace equation for the 2D droplet given by the following expression:

$$\Delta p = p_{\text{in}} - p_{\text{out}} = \frac{\sigma}{R}, \tag{46}$$

where R is the radius of the droplet, σ is the surface tension, and p_{in} and p_{out} are the pressure inside and outside the droplet, respectively. The pressure difference across the liquid-vapor interface is calculated at dimensionless temperatures $T = 0.4$ and $T = 0.5$ with the values of the surface tension coefficient $\kappa = 10^{-4}$ and $\kappa = 10^{-5}$ to verify the linear dependency of Δp and the inverse droplet radius $1/R$. Figure 16 illustrates Δp between the inside and the outside of the droplets as a function of the inverse droplet radius in the according conditions simulated using the present compact finite-difference LBM with the implementation of the SB and IB sensors in

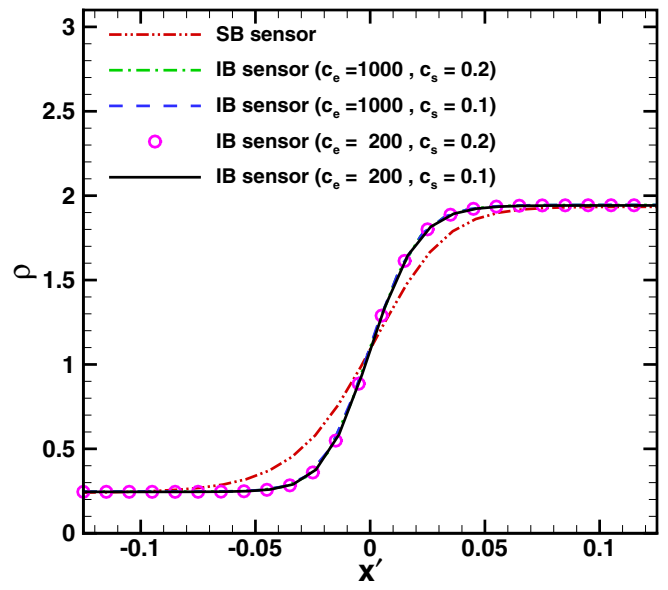

FIG. 14. (Color online) Effect of value of constants c_e and c_s in the IB sensor on density profiles at interfacial region of 2D droplet compared with result of SB sensor at temperature $T = 0.8$.

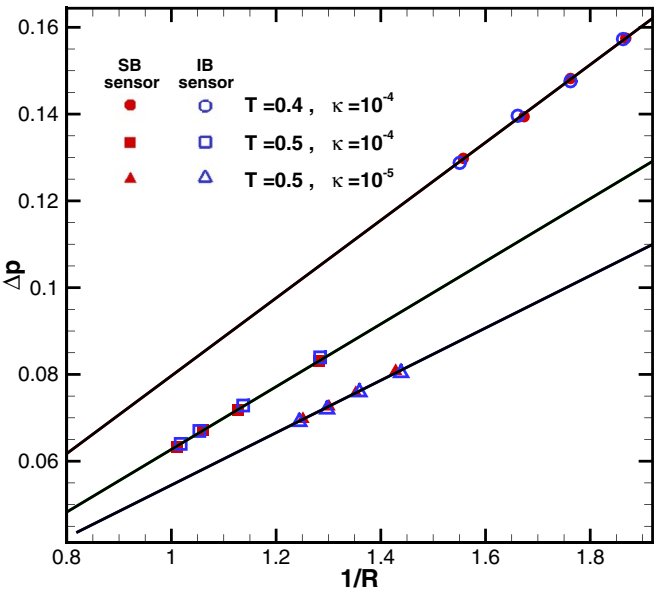

FIG. 16. (Color online) Verification of the Laplace law for a 2D droplet investigated by the present solution procedure using SB and IB sensors at different values of surface tension coefficient κ and temperature T.

the filtering scheme. It can be seen that the Laplace law is accurately satisfied for both the sensors and the linear relationship between Δp and $1/R$ confirms a constant value of the surface tension σ, representing the slope of the lines. From Fig. 16, it can be also concluded that there are two factors which determine the surface tension of the droplets, the surface tension coefficient κ, and the density gradient which is related to the temperature T. When $T = 0.5$, the runs of $\kappa = 10^{-4}$ and $\kappa = 10^{-5}$ are corresponding to the surface tensions $\sigma = 7.31 \times 10^{-2}$ and $\sigma = 6.18 \times 10^{-2}$, respectively. It shows that with decreasing the surface tension coefficient κ, the surface tension is decreased because the increment of the density gradients caused by this operation is not as large as the effect of decreasing the value of κ (see Fig. 15). For the constant $\kappa = 10^{-4}$, with decreasing of the temperature from $T = 0.5$ to $T = 0.4$, the value of surface tension is increased from $\sigma = 7.31 \times 10^{-2}$ to $\sigma = 9.00 \times 10^{-2}$, respectively, because decreasing the value of temperature causes more density gradients in the interface. The increment of the surface tension with decreasing the temperature is the reason why the density profiles become sharper at low temperatures (see Fig. 12). The results obtained demonstrate the successful employment and robustness of the compact finite-difference LBM implemented for accurately simulating two-dimensional liquid-vapor systems with the curved interface and high density ratios.

C. Wettability

The contact between multiphase fluids and partial wetting surfaces is ubiquitous in nature and in a large class of industrial processes, ranging from water droplets on leaves or window panes to lubrication, painting, and coating processes. When a two-phase fluid flow meets a solid surface, a finite contact angle, known as the partial wetting, can be seen between the liquid-gas interface and the wall. Forming the wetting angle is due to the balance of the surface tension forces and it is driven toward an equilibrium state by the capillary forces. The simulation of the wetting angle between the two-phase liquid-gas fluids and the solid surfaces is an appropriate test case to verify various models for the multiphase flows because it involves wall boundary conditions and intermolecular forces between the fluid and solid molecules.

Herein, a liquid droplet located between two parallel flat plates at the equilibrium state is studied to demonstrate the robustness and efficiency of the high-order compact finite-difference LBM implemented for the simulation of the contact angle and surface wettability. The HSD model used here (proposed by He *et al.* [20]) does not involve the intermolecular forces at the solid-fluid interface. Rothman and Zaleski [75], Yiotis *et al.* [76], and recently Lin *et al.* [77] have suggested and applied a mathematical assumption to extend the original HSD model for the simulation of the intermolecular forces between the fluid and solid molecules. In this way, an effective value is assigned for the density of the solid ρ_s in the range between the gas density and the liquid density, $\rho_v < \rho_s < \rho_l$. Therefore, the attracting forces between the two-phase fluid particles and the molecules of the solid are controlled by the density of the solid surface ρ_s on the wall nodes. For a value of ρ_s close to the liquid density, the molecules of the liquid phase are attracted stronger by the solid surface, and, in contrast, if the value of ρ_s be close to the gas density, the solid surface will attract the particles of the gas phase. Therefore, depending on the value of ρ_s, different wetting angles can be formed between the liquid-gas interface and the solid surface. Although this assumption is a crude estimate of the true chemical constitution of the solid surface [76], it is adopted in order to take advantage of the mean-field approximation for the intermolecular potential by Rowlinson and Widom [55]. Similar approaches have been used by Bekri and Adler [78] for the Gunstensen LB model and also in the original LB model by Shan and Chen [11] through the solid-fluid interaction potential.

In the present study, the size of the rectangular domain is 1.0×0.5 with a 121×61 uniform computational grid. Periodic boundary conditions are applied to the left and right sides of the computational domain and the no-slip wall boundary condition is applied on the upper and lower plates. The wall boundary conditions are applied by using the approach described in the previous paragraph. The density of the solid nodes is defined by the value of ρ_s, and the wetting angle is investigated at different conditions depending on different values of ρ_s. The IB sensor is implemented in the filtering scheme for the numerical simulation of this test case and the time step, the relaxation factor, the surface tension coefficient, and the filtering parameter are set to be $\delta t = 10^{-4}$, $\tau = 10^{-4}$, $\kappa = 10^{-4}$, and $a_f = 0.49$, respectively. A square liquid droplet located between the two parallel solid plates is considered at the dimensionless temperature $T = 0.7$ as an initial condition in the middle of the 2D domain. Initially, the upper and bottom sides of the droplet are in direct contact with the solid plates and a value between the liquid and gas densities is considered for the solid nodes, $\rho_v < \rho_s < \rho_l$. With starting the solution, the density considered for the solid surface enters the calculations through Eq. (8) for the external force and affects the affinity of the solid to the fluid phases. When the system reaches to the equilibrium state, a contact angle is formed between the flat plates and the interface of the liquid-vapor two-phase flow depending on the value of ρ_s. The results for the equilibrium state of the square droplet between the two parallel plates calculated using the high-order compact finite-difference LBM implemented are depicted by the density contours in Fig. 17 at different normalized solid densities D_ρ, defined as:

$$D_\rho = \frac{\rho_s - \rho_v}{\rho_l - \rho_v}. \tag{47}$$

Figure 18 shows the wetting angle θ_w at the equilibrium state for the square droplet between the two parallel plates obtained by the present solution procedure for different values of the normalized solid density D_ρ. As shown in this figure, the wetting angle obtained by using the present solution algorithm has a linear dependence to the normalized solid density that is agreement with the results reported in the previous works [76,77]. As the value of solid density ρ_s increases from ρ_v to ρ_l, the solid surface changes from the gas-wet surface to the liquid-wet surface. Consequently, it is observed that the equilibrium wetting angle θ_w decreases with increasing the value of D_ρ in Figs. 17 and 18.

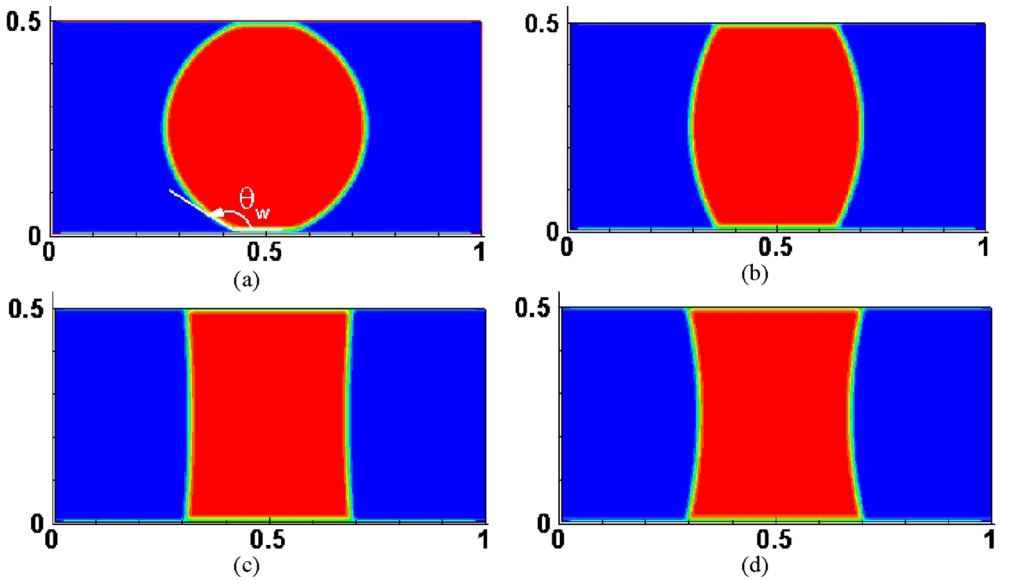

FIG. 17. (Color online) Computed density field of a square liquid droplet between two parallel flat plates at temperature $T = 0.7$ for normalized solid densities (a) $D_\rho = 0.2$, (b) $D_\rho = 0.5$, (c) $D_\rho = 0.8$, and (d) $D_\rho = 0.9$.

D. Coalescence of two droplets

In many two-phase flow applications such as boiling, emulsions, ink jets, as well as for rain in nature, the coalescence of bubbles or droplets arises. In the boiling water reactors (BWR), for example, the droplets in the vapor stream coalesce with other droplets or with the liquid films on the cladding. The study of these phenomena is a challenging task for accurately analyzing the thermodynamic of reactors. Explicitly, there are some difficulties for the numerical simulation of the coalescence phenomena by existing models, even with current CFD codes [35]. According to the efficiency of the LBM and its advantageous over traditional Navier-Stokes for the simulation of the multiphase flows, many researchers have been interested to solve the coalescence phenomena by using the LB method [8,26,35,79,80].

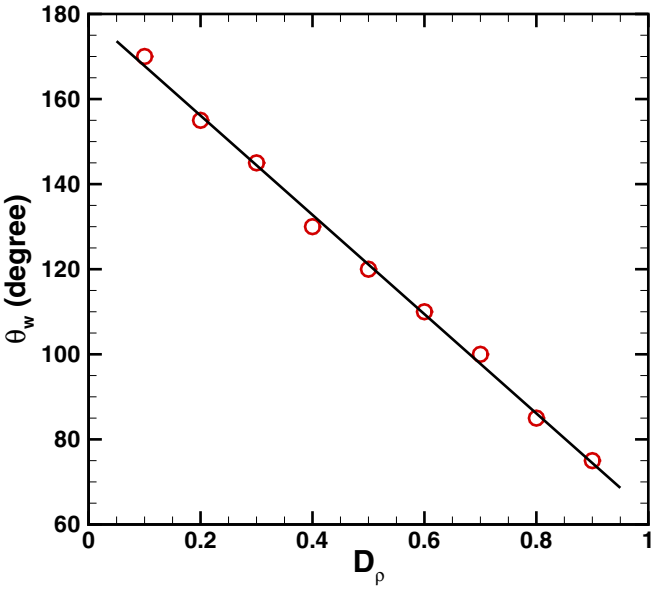

FIG. 18. (Color online) Computed wetting angle obtained by the present solution procedure for different normalized solid densities at temperature $T = 0.7$.

Here the numerical solution of the coalescence of two droplets is performed to demonstrate the accuracy and stability of the high-order CFDLBM employed for studying relatively complex two-phase flows with high density ratios. The flow parameters of the two droplets used for the numerical simulation of the coalescence phenomena are shown in Fig. 19. A $(L \times H) = (2.7 \times 2.0)$ rectangular domain with the uniform mesh (271×201) is used and periodic boundary conditions are applied to all the open boundaries at the four sides of the computational domain. The time step, the relaxation factor, and the surface tension coefficient are set to be $\delta t = 10^{-4}$, $\tau = 10^{-4}$, and $\kappa = 10^{-4}$, respectively, and the SB sensor is used in this study. For studying the coalescence phenomena with a large density ratio, two identical circular droplets of radius $r = 0.42$ with the density ratio $\rho_l/\rho_v = 961$ and the interface thickness $w = 0.064$ (corresponding to the dimensionless temperature $T = 0.4$) are placed close to each other in the center of the computational domain. The distance between the

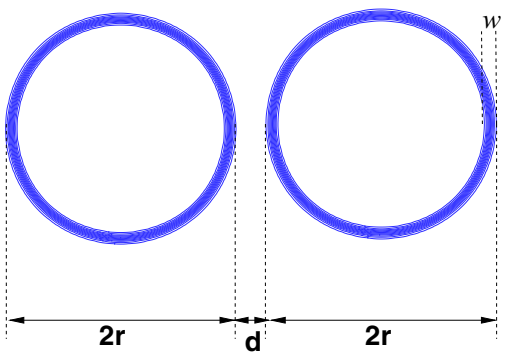

FIG. 19. (Color online) Flow parameters of two droplets used for numerical simulation of coalescence phenomena.

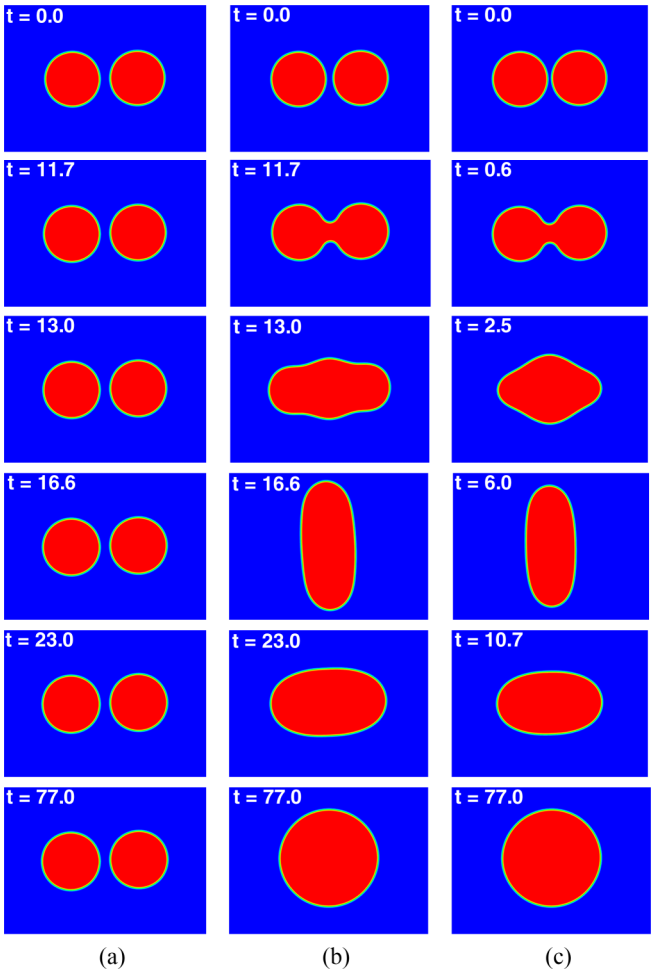

FIG. 20. (Color online) Snapshots of numerical results of droplet shapes in coalescence phenomena at distances (a) $d = 0.136$, (b) $d = 0.116$, and (c) $d = 0.076$.

two droplets d and the interface width w are the major factors that determine whether the droplets will merge together or not.

To study the effect of distance between the two droplets in the coalescence phenomena by using the solution methodology developed, three different gaps, $d = 0.136, 0.116$, and 0.076, are considered between the droplets. Figure 20 shows the snapshots of the numerical results of the droplet shapes obtained for different nondimensional times. It can be observed that the two droplets do not merge together when the gap of two droplets is set to be $d = 0.136$. This result is in agreement with the conclusion obtained by other researchers that when the gap of the two droplets is larger than twice the interface width $d > 2w$, they do not merge [35].

For the cases where the gap of two droplets is less than $2w$ ($d = 0.116, 0.076$), as the simulation starts, the inter-molecular forces cause the droplets to merge together eventually and the coalescence phenomenon occurs. It can be seen clearly that for $d = 0.116$ the merging process is much slower than in the case where $d = 0.076$. This study conducted also shows that the tension forces send the surface of the droplets into oscillation in the coalescence process before they merge to become a single circular droplet in the equilibrium state. It ensures that the surface tension effect is properly implemented in the solution algorithm. The results shown in Fig. 20 are very similar to those obtained by Sankaranarayanan [81], Yuan [80], Zheng *et al.* [35], and Reis and Phillips [79]. The reason that the results obtained in the present study differ qualitatively is that the density ratio as well as the surface tension of the droplets in this study differ from those they considered.

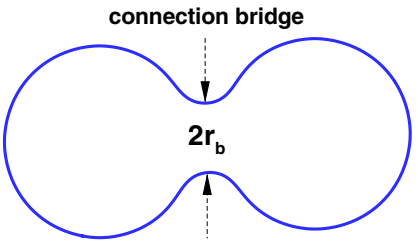

FIG. 21. (Color online) A schematic for coalescence of two droplets and connection bridge radius r_b.

When the coalescence starts and the two droplets come in contact, a connection bridge initially forms between the two droplets [82,83]. This bridge then gets pulled out by the surface tension force. A schematic for the coalescence of two droplets and the connection bridge radius r_b is shown in Fig. 21. The time evolution of the connection bridge radius r_b is shown in Fig. 22 for $d = 0.116$ and $d = 0.076$. The oscillation during the coalescence process can be observed clearly in this figure which plots the value of r_b at $x = L/2$ as a function of the nondimensional time. It is important to note that the merging process is slower for $d = 0.116$; however, the amplitude of the oscillations is higher for this case compared to the case $d = 0.076$. The radius of the final droplet should be equal to $\sqrt{2}r$ [79,80]. As shown in Fig. 20, this relation is satisfied for the results obtained by using the present solution algorithm.

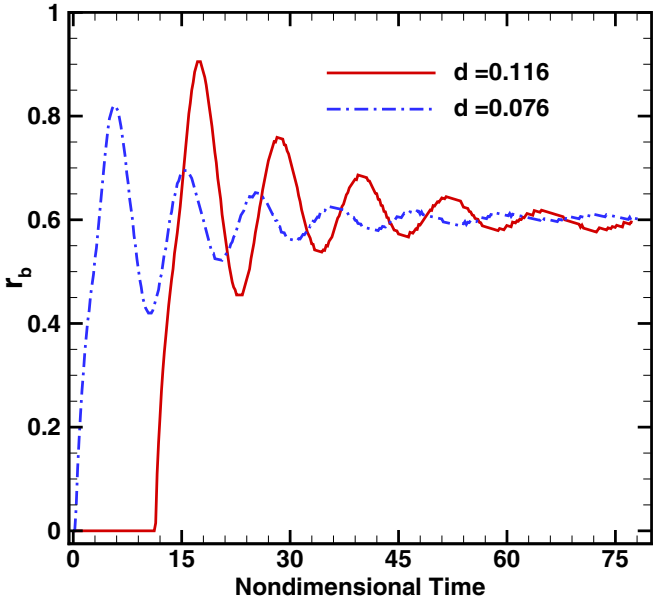

FIG. 22. (Color online) Time evolution of connection bridge radius r_b for coalescence of two droplets with distances $d = 0.116$ and $d = 0.076$.

The results obtained verify that the high-order finite difference LBM scheme is accurate and stable to simulate the two-phase phenomena with high-density ratio up to 1000.

E. Homogenous phase transition

When a homogenous vapor is quenched from above the critical temperature to below the critical point where two different phases can be coexist, the vapor phase becomes unstable and a part of it condenses into the liquid phase. This phase transition process is continued until the liquid and the vapor phases coexist in the equilibrium state. From a thermodynamic point of view, by decreasing the temperature at a constant volume, the kinetic energy of the molecules as well as the effect of collisions is reduced. Thus, the intermolecular forces become dominant in the vapor phase and small droplets begin to appear. Physically, the existence of some nuclei is necessary for the liquid phase to be formed in the homogenous vapor. These nuclei can be ions or submicroscopic particles which are naturally suspended in the vapor. The condensation of the vapor phase on the nuclei for establishing the liquid-vapor equilibrium is also called spinodal decomposition. Many researchers have been interested in studying this phenomenon using the multiphase LBM [11,30,52,84]. Here the phenomenon of the phase transition is performed in a 2D liquid-vapor system using the high-order compact finite-difference LBM implemented to demonstrate the stability and robustness of the present solution methodology for the simulation of such a complex test case. A 1×1 square domain with the uniform mesh (201×201) is used and periodic boundary conditions are applied to all the open boundaries at the four sides of the computational flow field ($0 \leqslant x, y \leqslant 1$). The time step and the relaxation factor are set to be $\delta t = 10^{-4}$ and $\tau = 10^{-4}$ respectively. Both the SB and IB sensors are used for the filtering scheme and the filtering coefficient set to be $a_f = 0.49$. The dimensionless temperature is set as $T = 0.7$, where the coexisting densities are $\rho_l = 2.146$ and $\rho_v = 0.1259$, and corresponds to the density ratio 17. The initial condition is determined with a random density distribution in the flow field at which the local density ρ is initialized with the small fluctuation 10% about the mean density ρ_c. This statistical perturbation is necessary to induce the phase transition in the flow field, since the random noise of the amplitude $0.1\rho_c$ representing the nuclei in the density field and the vapor phase begin to condense on these nuclei when the system is quenched from the critical point to the temperature $T = 0.7$. The sequence of the phase transition is shown by the density field for three different surface-tension coefficients $\kappa = 10^{-4}, 10^{-5}$, and 10^{-6} at the consecutive times in Figs. 23 and 24 by applying the SB and IB sensors in the filtering scheme, respectively. The calculations are performed

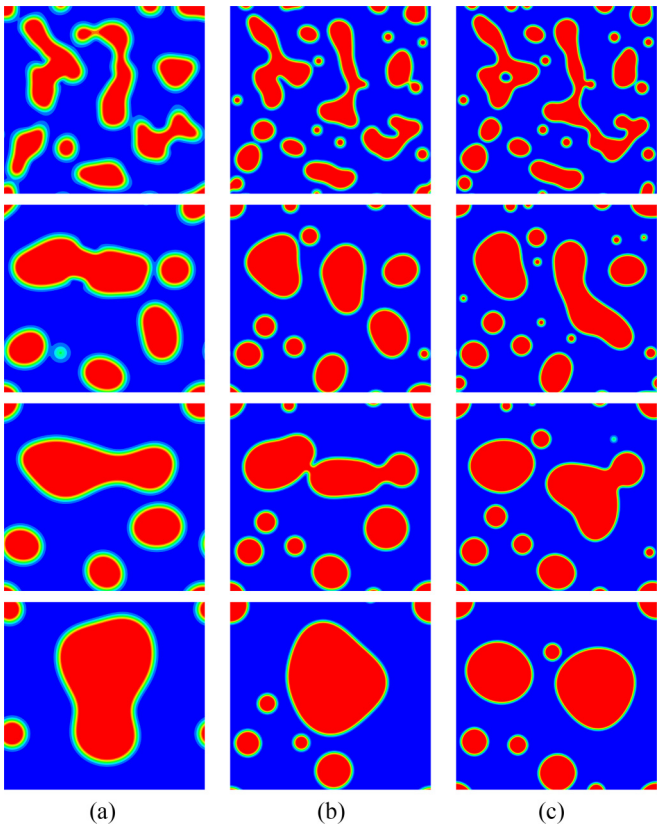

FIG. 23. (Color online) Computed density field of 2D phase separation in a liquid-vapor system using SB sensor at temperature $T = 0.7$ at times $t = 0.4$ (first row), $t = 1.2$ (second row), $t = 2.0$ (third row), and $t = 5.2$ (fourth row) for surface tension coefficients (a) $\kappa = 10^{-4}$, (b) $\kappa = 10^{-5}$, and (c) $\kappa = 10^{-6}$.

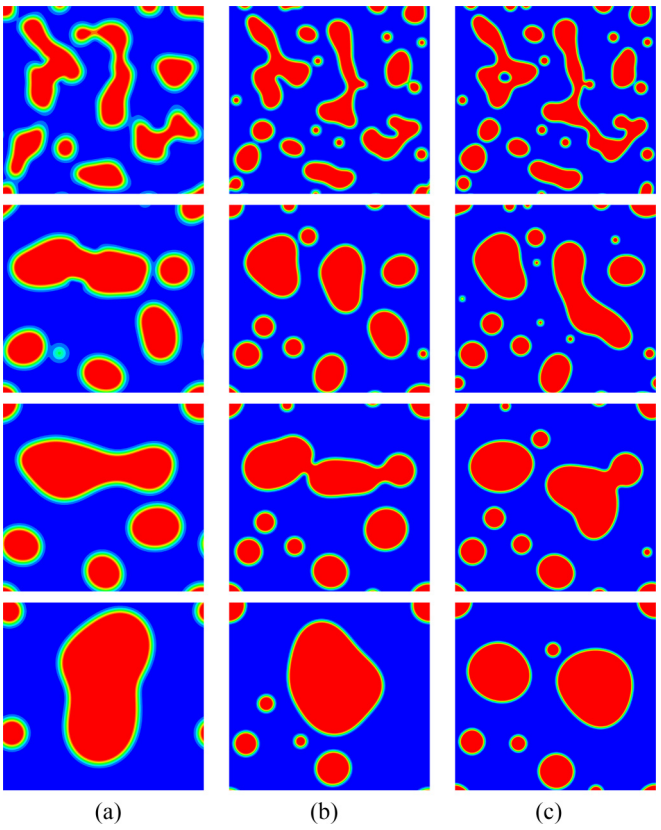

FIG. 24. (Color online) Computed density field of 2D phase separation in a liquid-vapor system using IB sensor at temperature $T = 0.7$ at times $t = 0.4$ (first row), $t = 1.2$ (second row), $t = 2.0$ (third row), and $t = 5.2$ (fourth row) for surface tension coefficients (a) $\kappa = 10^{-4}$, (b) $\kappa = 10^{-5}$, and (c) $\kappa = 10^{-6}$.

TABLE V. Computation time for different liquid-vapor two-phase flows investigated by the high-order compact finite-difference LBM implemented.

Test case	Test condition	Sensor	Computational time (hr)
Liquid-vapor system with planar interface	$T = 0.8$ Grid (121×61)	SW	0.58
		SB	0.65
		IB	0.73
	$T = 0.4$ Grid (121×61)	SW	–
		SB	0.80
		IB	0.87
Circular stationary droplet	$T = 0.8, \kappa = 10^{-4}$ Grid (201×201)	SB	2.09
		IB	2.48
	$T = 0.4, \kappa = 10^{-4}$ Grid (201×201)	SB	2.30
		IB	2.71
Coalescence of two droplets	$T = 0.4$ Grid (271×201)	SB	5.41
Homogenous phase transition	$T = 0.7, \kappa = 10^{-5}$ Grid (201×201)	SB	0.46
		IB	0.51
Liquid droplet located between two parallel flat plates	$T = 0.7, D_\rho = 0.5$ Grid (121×61)	IB	1.25

5.2 nondimensional times. With the start of the simulation, it is obvious that the spinodal decomposition occurs and the phases start to separate. The small droplets are coalescing and form a larger region filled with the liquid phase as the time evolves. The results obtained by applying the CFDLBM verify that the phase transition is quick in the beginning of the separation process, because the small droplets are more unstable than the greater ones. Thus, as the time evolves, the rate of phase separation becomes slower due to the large amount of small droplets competing for those particles which are still in the vapor phase. As previously explained, the parameter κ controls the surface tension and its value also affects the interface thickness in the liquid-vapor flows (see Figs. 15 and 16). As shown in Figs. 23 and 24, decreasing the surface tension coefficient κ denotes a decrease of the surface tension σ, the rate of coalescence of the droplets is slower. It is also clearly indicated that the thickness of the interface becomes larger as κ increases. The fourth-order compact finite-difference LBM implemented shows a good stability and robustness for solving two-phase flows and provides accurate and reliable solutions.

VII. COMPUTATIONAL COST

The computational cost required for the numerical simulation of the test cases presented in the paper using the high-order compact finite-difference LBM implemented is reported in Table V. The present numerical simulations are performed on a 3.2-GHz Pentium IV computer with a 64-bit operating system and 6-GB RAM. The computational time for each numerical simulation is measured depending on the dimensionless time required to achieve the equilibrium state or desired solution in the liquid-vapor systems studied. Each numerical simulation required approximately 0.5–5 h, depending on the grid size used and the dimensionless time required in the liquid-vapor systems studied. As observed in Table V, the computational time for the IB sensor is slightly larger than the other sensors due to the additional calculations of the local and global scales in the filtering scheme used.

VIII. CONCLUDING REMARKS

A high-order CFDLBM is extended and applied to accurately simulate two-phase liquid-vapor flows with high density ratios. The He-Shan-Doolen-type lattice Boltzmann multiphase model is used and the discretization of the spatial derivatives in the resulting equations is performed by using the fourth-order compact finite-difference scheme and the discretization of the temporal term is made with the fourth-order Runge-Kutta scheme to provide an accurate and efficient two-phase flow solver. A filtering procedure is adopted and assessed for the stabilization of the solution algorithm. The calculations are performed for different two-phase liquid-vapor flow problems to demonstrate the accuracy and robustness of the high-order compact LBM applied. Some conclusions and remarks regarding the present study are as follows:

(1) It is shown that the computed results obtained by the CFDLBM for the two-phase flow problems simulated are in good agreement with the analytical and the numerical results reported in the literature. The study indicates that the solution procedure adopted here is accurate and robust for the test cases simulated for different conditions.

(2) A sensitivity study is performed to examine the accuracy and performance of the solution of the CFDLBM to the numerical parameters. The order of accuracy of the solution algorithm is verified through a grid refinement study. It is shown that the accuracy and the convergence rate of the equilibrium state solution of the two-phase flows by applying the compact finite-difference LBM implemented are not very sensitive to the value of filtering coefficient.

(3) A high-order spectral-type low-pass compact nonlinear filter with different sensors is used for the stabilization of the solution algorithm. Here three discontinuity-detecting sensors, namely the SW, SB, and IB sensors, for properly switching between a second-order and a higher-order filter are applied and assessed. It is shown that the filtering technique used can be conveniently adopted to reduce the spurious velocities and improve the numerical stability of the CFDLBM implemented in simulating two-phase flows with high density ratios. The study shows that all the three sensors provide nearly the same results, however, the performance of the SB and IB sensors in decreasing the level of the spurious velocities is better than the SW sensor. The results shows that the fourth-order compact finite-difference LBM by using the SB and IB sensors is accurate and robust for solving two-phase liquid-vapor flows even at high density ratios.

(4) The effects of different physical parameters, such as the surface tension and the temperature, are studied on the treatment of liquid-vapor two-phase flows in different conditions. The results obtained verify that the density ratio between the liquid and the vapor phase is only determined by the temperature.

(5) This study demonstrates that the present solution methodology is robust and accurate for solving two-phase liquid-vapor flow problems even at high density ratios. The solution procedure developed here can be used to provide benchmark solutions for the assessment of the accuracy of the other two-phase LBM-based flow solvers.

ACKNOWLEDGMENT

The authors thank Sharif University of Technology for supporting this research.

[1] L. M. Pismen, Phys. Rev. E **64**, 021603 (2001).
[2] D. M. Anderson, G. B. McFadden, and A. A. Wheeler, Annu. Rev. Fluid Mech. **30**, 139 (1998).
[3] R. R. Nourgaliev, T. N. Dinh, T. G. Theofanous, and D. Joseph, Int. J. Multiphase Flow **29**, 117 (2003).
[4] C. W. Hirt and B. D. Nichols, J. Comput. Phys. **39**, 201 (1981).
[5] S. Osher and J. A. Sethian, J. Comput. Phys. **79**, 12 (1988).
[6] S. O. Unverdi and G. Tryggvason, J. Comput. Phys. **100**, 25 (1992).
[7] T. Lee and C. L. Lin, Phys. Rev. E **67**, 056703 (2003).
[8] S. Gong and P. Cheng, Comput. Fluids **53**, 93 (2012).
[9] A. K. Gunstensen, D. H. Rothman, S. Zaleski, and G. Zanetti, Phys. Rev. A **43**, 4320 (1991).
[10] D. H. Rothman and J. M. Keller, J. Stat. Phys. **52**, 1119 (1988).
[11] X. Shan and H. Chen, Phys. Rev. E **47**, 1815 (1993).
[12] X. Shan and G. Doolen, J. Stat. Phys. **81**, 379 (1995).
[13] P. Yuan and L. Schaefer, Phys. Fluids **18**, 042101 (2006).
[14] L. S. Luo, Phys. Rev. E **62**, 4982 (2000).
[15] M. R. Swift, W. R. Osborn, and J. M. Yeomans, Phys. Rev. Lett. **75**, 830 (1995).
[16] M. R. Swift, E. Orlandini, W. R. Osborn, and J. M. Yeomans, Phys. Rev. E **54**, 5041 (1996).
[17] R. R. Nourgaliev, T. N. Dinh, and B. R. Sehgal, Nucl. Eng. Des. **211**, 153 (2002).
[18] X. He and G. D. Doolen, J. Stat. Phys. **107**, 309 (2002).
[19] L. S. Luo, Phys. Rev. Lett. **81**, 1618 (1998).
[20] X. He, X. Shan, and G. D. Doolen, Phys. Rev. E **57**, R13(R) (1998).
[21] X. He, S. Chen, and R. Zhang, J. Comput. Phys. **152**, 642 (1999).
[22] R. Zhang, X. He, and S. Chen, Comput. Phys. Commun. **129**, 121 (2000).
[23] R. Zhang, X. He, G. Doolen, and S. Chen, Adv. Water Resour. **24**, 461 (2001).
[24] Y. Chen, S. Teng, T. Shukuwa, and H. Ohashi, Int. J. Mod. Phys. C **09**, 1383 (1998).
[25] S. Teng, Y. Chen, and H. Ohashi, Int. J. Heat and Fluid Flow **21**, 112 (2000).
[26] T. Lee and P. F. Fischer, Phys. Rev. E **74**, 046709 (2006).
[27] A. Cristea and V. Sofonea, Int. J. Mod. Phys. C **14**, 1251 (2003).
[28] A. Cristea, G. Gonnella, A. Lamura, and V. Sofonea, Math. Comput. Simulat. **72**, 113 (2006).
[29] S. Lishchuk, C. Care, and I. Halliday, Phys. Rev. E **67**, 036701 (2003).
[30] V. Sofonea, A. Lamura, G. Gonnella, and A. Cristea, Phys. Rev. E **70**, 046702 (2004).
[31] A. J. Wagner, Int. J. Mod. Phys. B **17**, 193 (2003).
[32] X. Shan, Phys. Rev. E **73**, 047701 (2006).
[33] R. Scardovelli and S. Zaleski, Annu. Rev. Fluid Mech. **31**, 567 (1999).
[34] T. Inamuro, T. Ogata, S. Tajima, and N. Konishi, J. Comput. Phys. **198**, 628 (2004).
[35] H. W. Zheng, C. Shu, and Y. T. Chew, J. Comput. Phys. **218**, 353 (2006).
[36] T. Lee and C. L. Lin, J. Comput. Phys. **206**, 16 (2005).
[37] K. Mattila, D. N. Siebert, L. A. Hegele, and P. C. Philippi, Int. J. Mod. Phys. C **24**, 1340006 (2013).
[38] T. Lee and G. K. Leaf, Eur. Phys. J. Spec. Top. **171**, 3 (2009).
[39] M. B. Reider and J. D. Sterling, Comput. Fluids **24**, 459 (1995).
[40] R. Mei and W. Shyy, J. Comput. Phys. **143**, 426 (1998).
[41] Z. Guo and T. S. Zhao, Phys. Rev. E **67**, 066709 (2003).
[42] V. Sofonea and R. F. Sekerka, J. Comput. Phys. **184**, 422 (2003).
[43] A. Xu, Phys. Rev. E **71**, 066706 (2005).
[44] S. C. Fu, R. M. C. So, and W. W. F. Leung, J. Comput. Phys. **229**, 6084 (2010).
[45] K. Hejranfar and E. Ezzatneshan, Int. J. Numer. Meth. Fluids **75**, 713 (2014).
[46] K. Hejranfar and E. Ezzatneshan, J. Comput. Phys. **267**, 28 (2014).
[47] P. Bhatnagar, E. P. Gross, and M. Krook, Phys. Rev. **94**, 511 (1954).
[48] N .S. Martys, X. Shan, and H. Chen, Phys. Rev. E **58**, 6855 (1998).
[49] A. Cristea, Int. J. Mod. Phys. C **17**, 1191 (2006).
[50] Y. H. Qian, D. d'Humières, and P. Lallemand, Europhys. Lett. **17**, 479 (1992).
[51] S. Chen and G. D. Doolen, Annu. Rev. Fluid Mech. **30**, 329 (1998).
[52] A. Cristea, G. Gonnella, A. Lamura, and V. Sofonea, Commun. Comput. Phys. **7**, 350 (2010).
[53] J. C. Maxwell, Nature **11**, 357 (1875).
[54] D. A. Wolf-Gladrow, *Lattice-Gas Cellular Automata and Lattice Boltzmann Models - An Introduction* (Springer, Berlin, 2000).

[55] J. S. Rowlinson and B. Widom, *Molecular Theory of Capillarity* (Clarendon Press, Oxford, 1982).
[56] B. Sanderse and B. Koren, J. Comput. Phys. **231**, 3041 (2012).
[57] R. S. Hirsch, J. Comput. Phys. **19**, 90 (1975).
[58] S. K. Lele, J. Comput. Phys. **103**, 16 (1992).
[59] M. H. Carpenter, D. Gottlieb, and S. Abarbanel, J. Comput. Phys. **108**, 272 (1993).
[60] M. R. Visbal and D. V. Gaitonde, J. Comput. Phys. **181**, 155 (2002).
[61] D. Ricot, S. Marié, P. Sagaut, and C. Bailly, J. Comput. Phys. **228**, 4478 (2009).
[62] R. A. Brownlee, J. Levesley, D. Packwood, and A. N. Gorban, Progr. Comput. Phys. **3**, 31 (2013).
[63] M. R. Visbal and D. V. Gaitonde, AIAA J. **37**, 1231 (1999).
[64] H. C. Yee, N. D. Sandham, and M. J. Djomehri, J. Comput. Phys. **150**, 199 (1999).
[65] B. Sjogreen and H. C. Yee, Comput. Fluids **37**, 593 (2008).
[66] M. R. Visbal and D. V. Gaitonde, AIAA paper2005-1265, (2005).
[67] C. Bogey, N. Cacqueray, and C. Bailly, J. Comput. Phys. **228**, 1447 (2009).
[68] H. Mahmoodi Darian, V. Esfahanian, and K. Hejranfar, J. Comput. Phys. **230**, 494 (2011).
[69] D. V. Gaitonde, J. S. Shang, and J. L. Young, Int. J. Numer. Meth. Eng. **45**, 1849 (1999).
[70] A. J. Wagner, Phys. Rev. E **74**, 056703 (2006).
[71] S. Hou, X. Shan, Q. Zou, G. D. Doolen, and W. E. Soll, J. Comput. Phys. **138**, 695 (1997).
[72] C. M. Pooley and K. Furtado, Phys. Rev. E **77**, 046702 (2008).
[73] H. Huang, L. Wang, and X. Lu, Comput. Math. Appl. **61**, 3606 (2011).
[74] A. Cristea, Proc. Rom. Acad., Ser. A **12**, 71 (2011).
[75] D. H. Rothman and S. Zaleski, *Lattice-Gas Cellular Automata* (Cambridge University Press, Cambridge, 1997).
[76] A. G. Yiotis, J. Psihogios, M. E. Kainourgiakis, A. Papaioannou, and A. K. Stubos, Colloids Surf. A **300**, 35 (2007).
[77] C. L. Lin, A. R. Videla, and J. D. Miller, Flow Meas. Instrum. **21**, 255 (2010).
[78] S. Bekri and P. M. Adler, Int. J. Multiphase Flow **28**, 665 (2002).
[79] T. Reis and T. N. Phillips, J. Phys. A: Math. Theor. **40**, 4033 (2007).
[80] P. Yuan, Ph.D. thesis, University of Pittsburgh, 2005.
[81] K. Sankaranarayanan, Ph.D. thesis, Princeton University, 2002.
[82] D. Li, J. Colloid Interface Sci. **181**, 34 (1996).
[83] D. S. Martula, R. T. Bonnecaze, and D. R. Lloyd, Int. J. Multiphase Flow **29**, 1265 (2003).
[84] W. R. Osborn, E. Orlandini, M. R. Swift, J. M. Yeomans, and J. R. Banavar, Phys. Rev. Lett. **75**, 4031 (1995).